APPLIED SCIENCES AND ENGINEERING

A 3D biomimetic optoelectronic scaffold repairs cranial defects

Huachun Wang[1], Jingjing Tian[2], Yuxi Jiang[3], Shuang Liu[4], Jingchuan Zheng[5], Ningyu Li[3], Guiyan Wang[3], Fan Dong[3], Junyu Chen[1], Yang Xie[1], Yunxiang Huang[1], Xue Cai[1], Xiumei Wang[5], Wei Xiong[4,6], Hui Qi[7], Lan Yin[5], Yuguang Wang[3]*, Xing Sheng[1,6]*

Bone fractures and defects pose serious health-related issues on patients. For clinical therapeutics, synthetic scaffolds have been actively explored to promote critical-sized bone regeneration, and electrical stimulations are recognized as an effective auxiliary to facilitate the process. Here, we develop a three-dimensional (3D) biomimetic scaffold integrated with thin-film silicon (Si)–based microstructures. This Si-based hybrid scaffold not only provides a 3D hierarchical structure for guiding cell growth but also regulates cell behaviors via photo-induced electrical signals. Remotely controlled by infrared illumination, these Si structures electrically modulate membrane potentials and intracellular calcium dynamics of stem cells and potentiate cell proliferation and differentiation. In a rodent model, the Si-integrated scaffold demonstrates improved osteogenesis under optical stimulations. Such a wirelessly powered optoelectronic scaffold eliminates tethered electrical implants and fully degrades in a biological environment. The Si-based 3D scaffold combines topographical and optoelectronic stimuli for effective biological modulations, offering broad potential for biomedicine.

INTRODUCTION

Every year, more than millions of patients suffer from bone diseases such as fractures, traumatic injury, and congenital disabilities (*1*). As a severe public health issue worldwide, bone diseases lead to deformity, long-term hospitalization, deteriorated life quality, and higher risks of death, associated with increasing economic burdens (*2*, *3*). Although the natural bone tissue has the inherent capability for rehabilitation via a self-regeneration process in response to minor damage, large fractures or massive defects make it difficult to achieve complete functional restoration without surgical intervention (*4*). One of the standard approaches to regenerating critical-sized bone defects relies on autografts, which not only have ideal osteoconductive and osteoinductive properties toward bone formation in the defect areas but also impose constraints including their limited availability and high risks of donor site morbidity (*5*). To overcome the above limitations of autografts, the synthetic biological scaffold (bio-scaffold) offers a promising alternative treatment for bone tissue engineering, functioning as substitutes filled in the defects and providing topographic support for cell adhesion, growth, and differentiation via mimicking extracellular matrix microenvironments (*6*, *7*). Tremendous efforts have focused on preparing desirable platforms from the aspect of materials, structures, and biofunctionality strategies to promote osteoregenerative properties for bio-scaffolds (*8–10*).

Advanced scaffolds inspired from natural bone tissues with three-dimensional (3D) hierarchical structures have been extensively exploited and applied for bone regeneration (*11*). In particular, mineralized materials lead the way forward in developing biological scaffolds for their structural and compositional bionic features (*12*). On one hand, mineralized scaffolds comprise multiple compositions including collagens, bioceramics [e.g., hydroxyapatite (HA)], and synthetic polymers [e.g., poly(ε-caprolactone) (PCL)], forming the main components of natural bone (*13*, *14*). On the other hand, they equip with multilevel bone-like hierarchical structures, ranging from micrometer to nanometer scales (*15*). These conventional scaffolds provide topographical and mechanical supports for cell growth and differentiation. In terms of additional biofunctionality, biochemical (growth factors, drugs, etc.) and physical (electrical, thermal, optical, magnetic, etc.) stimuli are used to potentiate bioactivities of inert synthetic scaffolds for osteogenesis (*8*, *16*). Compared with biochemical cues, physical cues offer high spatial and temporal resolutions and more stable and controllable operations when interacting with biosystems (*17–19*). Specifically, electrical transduction signals are the basis of biological activity, and provoking the endogenous electric fields of bone tissues with external electrical stimulation has been widely adopted for accelerating bone regeneration even in clinical scenarios to cure intractable delayed and nonunion bone fractures (*20*).

Traditional electrical therapies utilize direct current or alternating current stimulations for bone regeneration, involving implantable electrodes tethered to control circuit and power supplies (*21*, *22*). Recently, researchers have also investigated electrically active materials and devices that can be wirelessly or self-powered based on photocapacitors (*23*), electrostatics (*24*), and piezoelectronics (*25*). While these works demonstrate capabilities to modulate various types of cells (*26–28*) and tissues (*29*, *30*) for research and

[1]Department of Electronic Engineering, Beijing National Research Center for Information Science and Technology, Institute for Precision Medicine, Center for Flexible Electronics Technology, Tsinghua University, Beijing 100084, China. [2]Department of Medical Science Research Center, Peking Union Medical College Hospital, Chinese Academy of Medical Sciences & Peking Union Medical College, Beijing 100730, China. [3]National Engineering Laboratory for Digital and Material Technology of Stomatology, Peking University School and Hospital of Stomatology, Beijing 100082, China. [4]School of Life Sciences, Tsinghua University, Beijing 100084, China. [5]School of Materials Science and Engineering, State Key Laboratory of New Ceramics and Fine Processing, Key Laboratory of Advanced Materials of Ministry of Education, Tsinghua University, Beijing 100084, China. [6]IDG/McGovern Institute for Brain Research, Tsinghua University, Beijing 100084, China. [7]Beijing Research Institute of Traumatology and Orthopaedics, Beijing Jishuitan Hospital, Beijing 100035, China.
*Corresponding author. Email: wangyuguang@bjmu.edu.cn (Y.W.); xingsheng@tsinghua.edu.cn (X.S.)

therapeutic purposes (*31*, *32*), the interplay between optical/electrical signals and stem cell activities during the bone regeneration process has been less exploited. In addition, it would be highly desirable to realize a scaffold that can (i) mimic the hierarchical bone structures, (ii) generate wirelessly powered electrical signals and influence cell behaviors, and (iii) be fully compatible and degradable within the biological environment. We perceive that such an electrically active bio-scaffold can be explored for tissue regeneration and enable broad applications in biomedicine.

In this study, we present a 3D biodegradable optoelectronic bio-scaffold for bone tissue regeneration. The fabricated scaffold combines patterned silicon (Si) thin films embedded into HA mineralized collagen/PCL structures that can be fully dissolved in the biological environment. When culturing human bone marrow–derived mesenchymal stem cells (hBMSCs), the biomimetic multiscale hierarchical architecture offers favorable topographical supports for cell adhesion, growth, and differentiation. Responding to near–infrared (IR) illumination, the Si structures generate electrical signals that depolarize cell potentials and evoke intracellular calcium activities. These optoelectronic signals further regulate hBMSCs toward osteogenic differentiation. Last, in vivo experiments show that the Si-based bio-scaffold promotes the regeneration of cranial defects in a rodent model.

RESULTS

3D biomimetic optoelectronic scaffold with Si nanostructures

We propose a 3D biomimetic optoelectronic scaffold for repairing cranial bone defects in a rodent model, as illustrated in Fig. 1A. The implantable hybrid scaffold comprises thin-film Si nanostructures that generate electrical signals and interact with the tissue under extracranial illumination. Meanwhile, the 3D hierarchical structure provides a favorable microenvironment for tissue regeneration. As shown in Fig. 1B, the natural bone displays a typical multiscale architecture. Microscopically, it comprises compact bone (outer regions) and spongy bone (interior regions). Spongy bone (also known as cancellous bone) consists of a 3D trabeculae matrix with mixed mineralized collagen fibrils and plate-like HA crystals at the nanoscale level (*10*). Such a porous structure plays a crucial role in the biosystem for minerals and bone marrow storage, as well as erythropoiesis (*33*). Inspired by this structure, we design a 3D hybrid bio-scaffold that structurally emulates natural bone at the micro- and nanoscales (Fig. 1C). Here, the collagen/PCL composite mineralized by HA nanocrystals constitutes the porous matrix. Patterned monocrystalline Si films embed into the mineralized collagen/PCL scaffold and endow it with optoelectronic stimulations for bone regeneration. The rationally designed Si film presents a hierarchical structure, including a mesh structure at a scale of a few micrometers, as well as microscale pillars and nanoscale pyramids to physically regular the cellular behaviors.

On the basis of the above design, we construct the 3D hybrid scaffold (Fig. 2A), with fabrication details provided in Materials and Methods and fig. S1. To match the artificial cranial defects created for in vivo experiment, the formed scaffold has a disk shape with a diameter of ~5 mm and a thickness of ~0.8 mm. The porous mineralized collagen/PCL structure (*13*) serves as a host material, which includes thin-film p-type Si meshes with a thickness of ~3 μm and a gap size of ~200 μm. Lithographically

patterning and plasma etching form microscale pillar structures, and subsequent wet chemical etching further defines the nanoscale textured surface. The micro- and nanostructures notably enhance the overall optical absorption of the Si film (fig. S2) (*34*), thereby improving the photoelectric conversion efficiency for biological modulation. Furthermore, the embedded Si film increases the elastic modulus of the scaffold from 12 to 66 MPa (fig. S3), showing a better match with the mechanical strength of natural porous bone (20 to 450 MPa) (*35*).

Figure 2 (B and C) presents the scanning electron microscopic (SEM) and confocal fluorescence images for hBMSCs cultured on the scaffold. The SEM image shows that the hBMSCs enter into the 3D porous structure and attach well on the patterned Si surface as well as the mineralized scaffold. In addition, the hBMSCs present a well-spreading, elongated, and typical spindle-like morphology on both surfaces, indicating that the 3D hybrid scaffold provides a desirable microenvironment for cell attachment and growth. Moreover, both the host material (PCL) and thin-film Si are degradable in a biological environment, implicating their use in tissue regeneration (*36*, *37*). Since compositional materials of the scaffold would take a long time to naturally disappear in the physiological condition at 37°C [for example, 1 to 2 years for PCL (*38*) and 3 to 6 months for Si (*39*)], we evaluate the accelerated dissolution process of the scaffold immersed in the phosphate-buffered saline (PBS) solution at 60°C (Fig. 2D). The Si thin-film component is fully absorbed after immersion for 4 days. After 8 days, the main body of the scaffold is entirely disintegrated, leaving the mineralized collagen powders suspended in solution.

Effects of Si microstructures on behaviors of cultured hBMSCs

The microstructures in natural bone provide ideal mechanical transduction functions to effectively modulate cellular behaviors and promote the tissue growth (*40*). To mimic the complex biological tissue, patterned Si surfaces have been reported as a viable tool for regulating the growth, proliferation, and differentiation behaviors of stem cells (*41*, *42*). Here, we investigate the impacts of Si microstructures on the direction and osteogenesis process for cultured hBMSCs. Lithographical processes define micrometer-scale pillars (Fig. 2A) on one side of the monocrystalline Si sample, while the remaining area remains flat (Fig. 3A). After the sample surface is treated with polydopamine for improved hydrophilicity (fig. S4), hBMSCs are inoculated on the surfaces of Si pillars and planar Si, of which the topographical effects on the cell behaviors are compared side by side. Figure 3B presents an SEM image of hBMSCs cultured on the Si thin film for 24 hours, showing that the cells display distinct morphologies depending on the surface structures. Specifically, cells adhere on Si pillars with elongated body shape and numerous long filopodia-like protrusions, while those on the planar Si have a flat spindle shape and produce fewer and shorter protrusions. Further analyses are performed by imaging the fluorescence of actin cytoskeleton in hBMSCs stained with phalloidin at different time points (Fig. 3, C to E). After seeding for the first 1 hour, cells on Si pillars have multitudinous actin-enriched filopodia-like protrusions extended radially from nuclei, with a much higher density compared to cells on the planar Si film (Fig. 3C). After 3 hours, there are more cells that accumulate and adhere to Si pillars than to planar Si (Fig. 3D). Cultured cells continue to spread after 24 hours, and those on Si pillars present more prominent elongated
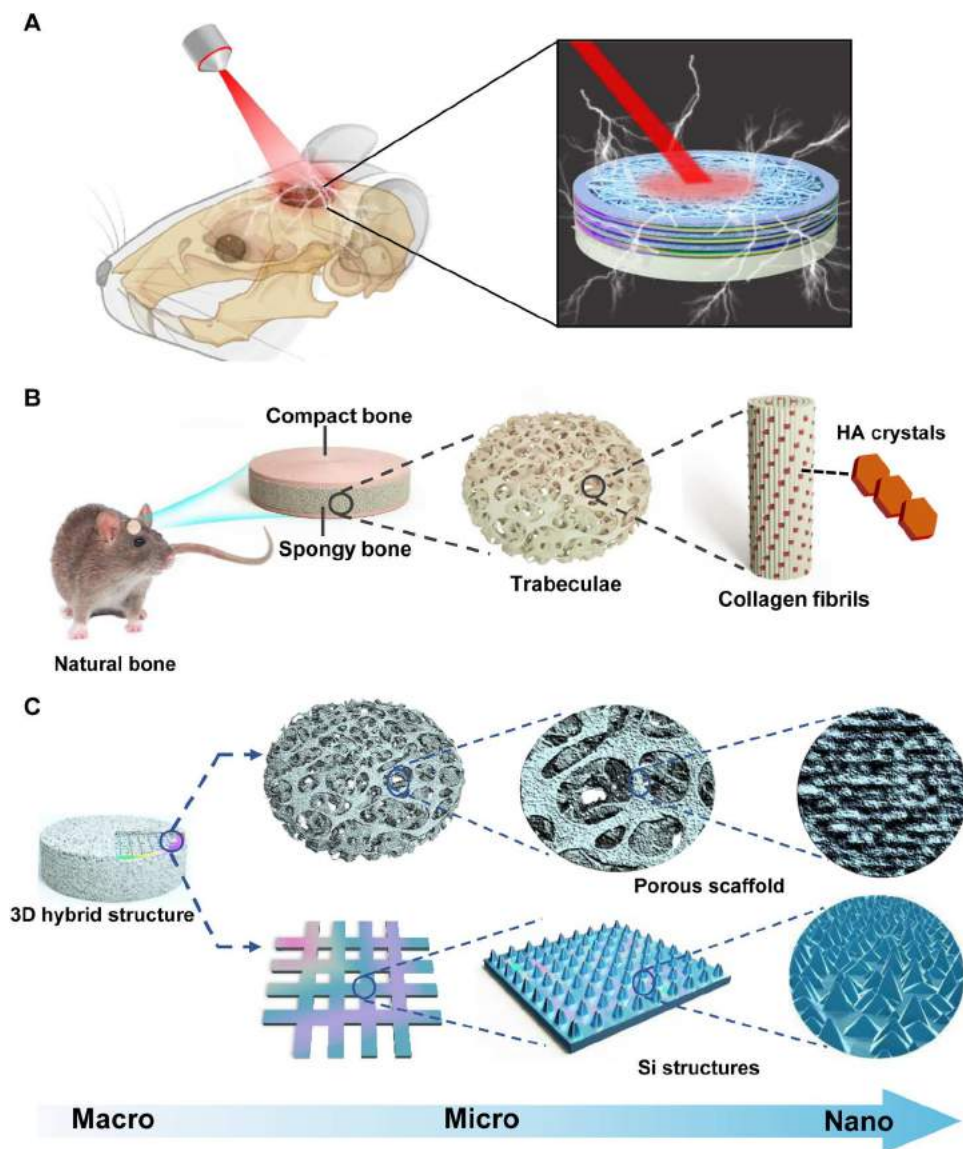
Fig. 1. Biomimetic strategy to construct a 3D optoelectronic scaffold with Si nanostructures for bone regeneration. (**A**) Conceptual illustration of the implantable scaffold for optically activated skull repairing. (**B**) Scheme of the hierarchical structure of the native bone, from macroscale to nanoscale. It comprises the compact bone on the surface and the spongy bone in the interior. The spongy bone is composed of a porous network of trabeculae consisting of collagen fibrils. (**C**) Biomimetic design of the 3D hybrid structure, incorporating a biodegradable porous collagen/HA/PCL scaffold (top) with embedded thin-film Si patterns with mesh, pillar, and pyramid structures at multiscale levels (bottom).

morphologies with longer protrusions (Fig. 3E). Schematically illustrated in Fig. 3F, the 3D topographic texture of the Si surface clearly affects cellular behaviors and markedly regulates cell morphologies cultured from 1 to 24 hours. Figure 3 (G to I) summarizes statistical analyses of geometrical characteristics obtained among multiple cells. hBMSCs preferentially adhere to and grow on Si pillars, exhibiting larger spread areas and more extended actin-rich membrane protrusions than those on planar Si. These microstructures also similarly interact with another type of preosteoblast cells (MC3T3-E1 cell line from mouse) (fig. S5). Compared with the planar Si, Si pillars help guide and promote the migration of MC3T3-E1 cells (fig. S6). Furthermore, we perform staining of alkaline phosphatase (ALP) (Fig. 3J) and alizarin red S (ARS)

(Fig. 3K) after culturing hBMSCs on Si samples for 7 and 14 days, respectively. On the same sample, the regions with Si pillars present deeper staining colors than planar Si, indicating a higher ALP activity and more calcium phosphate deposition induced by the 3D texture. Collectively, these cell culturing results suggest that the Si microstructures favorably modulate cell morphologies and promote their osteogenic activities.

Optoelectronic response of Si-based scaffolds in an aqueous solution

Our proposed 3D scaffold integrates patterned Si films, which produce photogenerated electrical signals under IR illumination and could potentially modulate biological activities in the
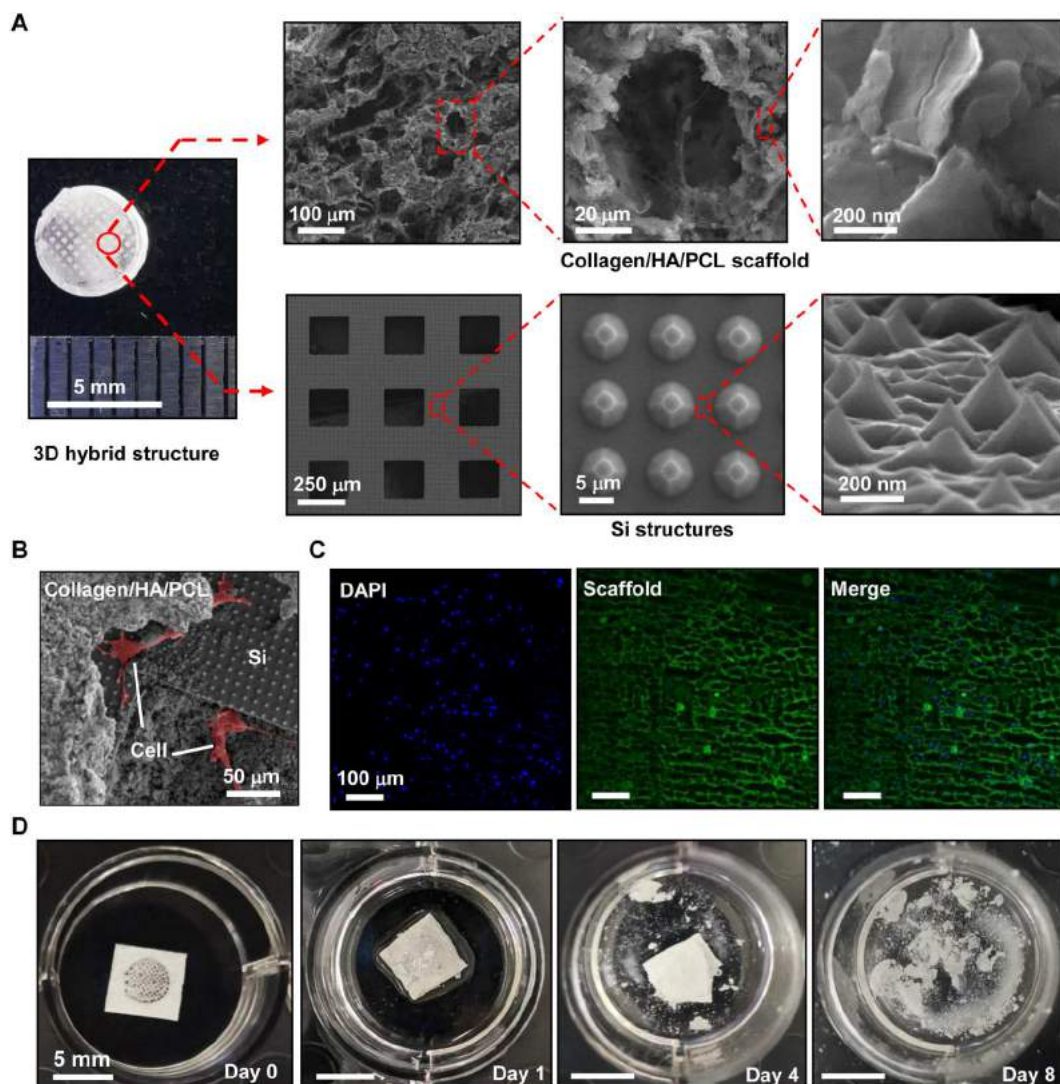
Fig. 2. Structures and degradation properties of the 3D optoelectronic scaffold. (**A**) Photo and SEM images of the hierarchical structure. Top: Porous mineralized collagen/HA/PCL scaffolds. Bottom: Thin-film Si structures. (**B**) SEM and (**C**) fluorescent images showing hBMSCs cultured on the scaffold [green: phalloidin staining for both scaffold and actin cytoskeleton; blue: nuclei stained with 4',6-diamidino-2-phenylindole (DAPI)]. (**D**) Images of the scaffold captured at different stages during the accelerated degradation, by immersion in the PBS (pH 7.4) at 60°C.

aqueous environment. In Fig. 4, we evaluate the photovoltage and photocurrent signals established by Si films in PBS, as well as their stabilities after chronic immersion. Via a standard patch-clamp technique (*30*), a glass pipette electrode is placed on the Si film and records photocurrents under illumination by an 808-nm laser (Fig. 4A). Figure 4B plots time-dependent photocurrents recorded for a scaffold with (w/; red) and without (w/o; black) the Si thin film (pulse width, 10 ms; frequency, 1 Hz). Under an illumination intensity of 200 mW/cm^2, the optoelectronic scaffold with Si produces a transient capacitive current with a peak value of ~1.6 nA, while the traditional mineralized scaffold exhibits no response. One can attribute this optoelectronic response to the build-in electric field established in the Si/solution heterojunction, which separates photogenerated carriers (electrons and holes) and causes ion accumulation at the interface (Fig. 4C). Figure 4D presents the photocurrent response collected for a floating Si film (without the

scaffold) under illumination at various intensities, showing that higher intensities lead to higher peak currents and faster decay. For biomedical applications such as tissue regeneration, desirable implants should operate effectively throughout a certain period of time before they are fully absorbed in the biological environment. It is known that crystalline Si films naturally dissolve in the biological environment at a rate of 10 to 100 nm/day (*43*, *44*), which would also cause the gradual degradation of their optoelectronic performance. We study degradation behaviors of Si films immersed in standard cell culture media at 37°C (Fig. 4E). After the immersion, the Si film retains ~80% of its initial photocurrents (at day 0) at day 14, and the currents decrease by ~80% at day 30. In addition, the optoelectronic performance of Si films also depends on the film thickness. Thicker Si films absorb more IR light and thus have higher photocurrent and photovoltage signals (fig. S7). To achieve
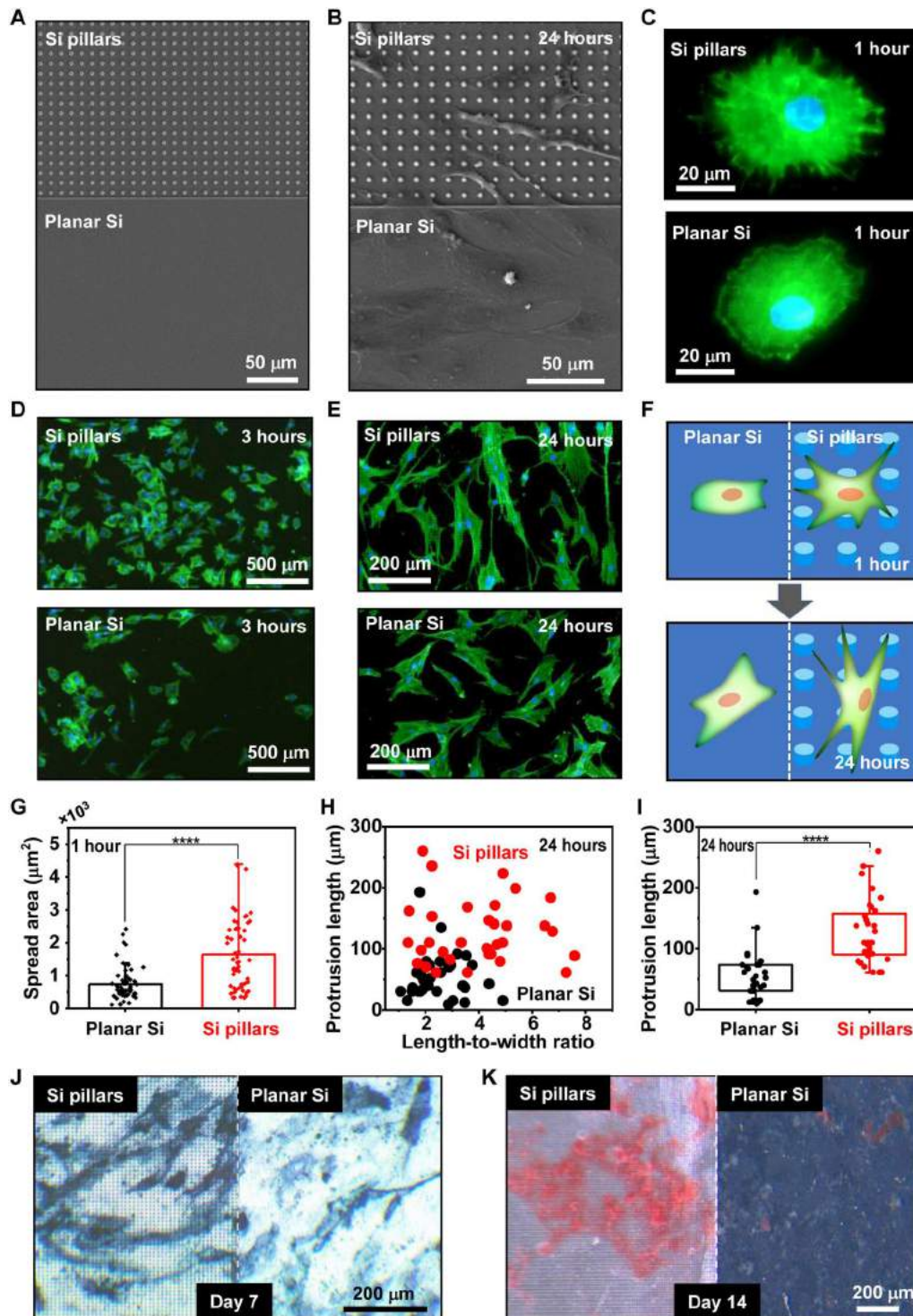
Fig. 3. Effects of Si microstructures on the morphological evolution and differentiation behaviors of hBMSCs. (**A**) SEM image (top view) of a sample with both patterns of Si pillars (top) and planar Si surfaces (bottom). (**B**) SEM image showing the sample with hBMSCs cultured for 24 hours. (**C**) Zoomed-in fluorescent images for hBMSCs cultured on Si pillars (top) and planar Si (bottom) for 1 hour. Green: actin cytoskeleton; blue: nucleus. (**D** and **E**) Fluorescence images showing massive hBMSCs on different Si surfaces cultured for (D) 3 hours and (E) 24 hours. (**F**) Schematic illustration of different cell morphologies on Si pillars and planar Si surfaces, respectively. (**G** to **I**) Quantitative analyses of geometrical features for hBMSCs cultured on different Si surfaces. (G) Spread area ($n = 58$ cells), (H) length-to-width ratio versus protrusion length ($n = 32$ cells), and (I) protrusion length ($n = 32$ cells); Student's t test, **** $P < 0.0001$. (**J**) Alkaline phosphatase (ALP) and (**K**) alizarin red S (ARS) staining for hBMSCs cultured on different Si surfaces for 7 and 14 days, respectively.
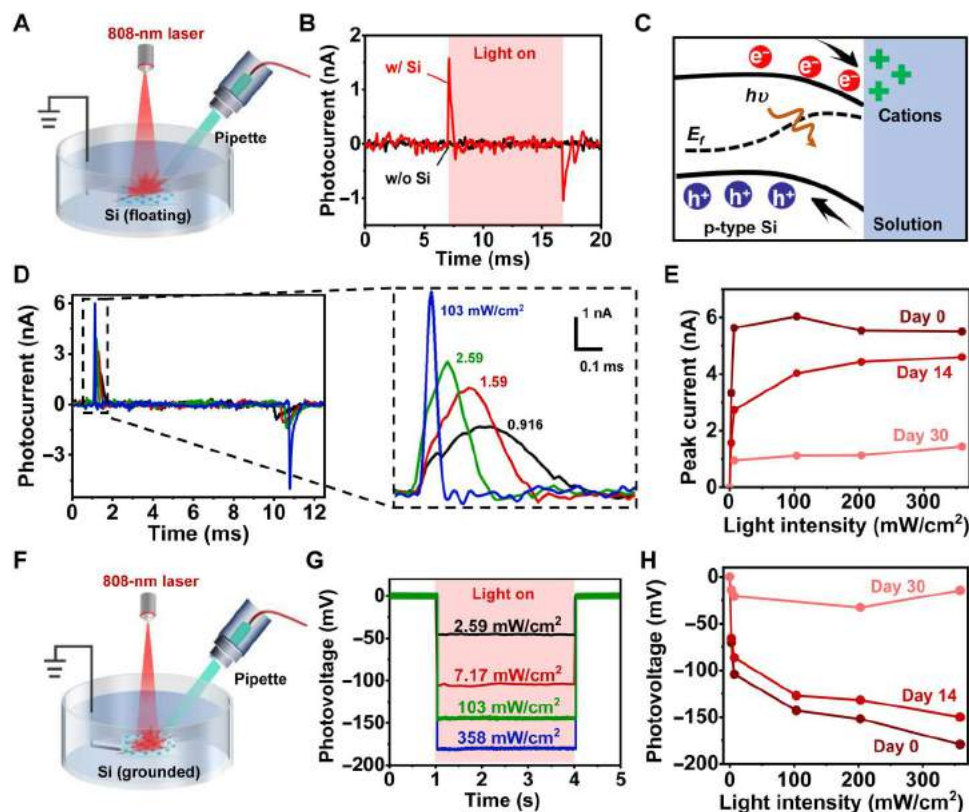
Fig. 4. In vitro optoelectronic response of 3D scaffolds. (**A**) Scheme for the photocurrent measurement for scaffold samples floating in the PBS. A pipette electrode is connected to a patch-clamp setup and positioned close (3 to 5 μm) to the sample surface. The light (808 nm laser, ~4 mm spot size) is normally incident on the sample surface. (**B**) Photocurrent responses for 3D scaffolds with (red) and without (black) Si films. The illumination condition is as follows: pulse width, 10 ms; intensity, 200 mW/cm^2; frequency, 1 Hz. (**C**) Schematic energy diagram illustrating the carrier generation and separation in the Si film, as well as the ion accumulation at the Si/solution interface. (**D**) Left: Photocurrent responses for Si films under illumination with different light intensities (10-ms pulse, 1 Hz). Right: Exploded view of the peak currents. (**E**) Peak current versus light intensity and performance degradation after immersing the Si films in the cell culture medium for different times. (**F**) Scheme of the photovoltage measurement for Si samples in the PBS solution. The backside of Si film is grounded with the recording electrode. (**G**) Measured photovoltage responses for Si films under illumination with different light intensities (3-s continuous illumination). (**H**) Photovoltage versus light intensity and performance degradation after immersion in the cell culture medium.

a trade-off between the optical response and the biodegradation, we select 3-μm-thick Si films for in vivo studies.

We also capture steady-state photovoltages generated in the Si/solution junction by grounding the Si film with backside electrodes (Fig. 4F). Dynamically responding to a continuous (3 s) irradiation at intensities from 2.59 to 358 mW/cm^2, recorded steady-state voltages range from −46 to −180 mV (Fig. 4G). The negative voltage values are in accordance with the band structure of the Si/solution junction illustrated in Fig. 4C. The photovoltage degradation trend is also consistent with the results in Fig. 4E, showing a voltage decrease of ~15% after 14-day immersion (Fig. 4H). The sustained optoelectronic performance during the first 14-day immersion ensures that the Si structures would effectively function during the initial stage of cell proliferation and osteogenesis. The photogenerated voltage signals could induce redox reactions and create reactive oxygen species (ROS) at the Si/solution interface (26, 45). Fluorescence recordings with a chemical probe [2,7-dichloro-dihydro-fluorescein (DCFH)] confirm the increased level of ROS associated with optoelectronic stimulations on Si films (fig. S8). As chemical cues, these ROS products play essential roles in

signal transduction, cell modulation, and tissue regeneration (32, 46, 47).

Photoinduced electrophysiological and calcium activities of hBMSCs on Si films in vitro

In biosystems, endogenous electrical fields participate in many important processes including embryonic development, wound and tissue regeneration, and remolding (48). Although electrical stimulations have been extensively exploited to regulate neural and cardiac cells and systems, their effects on nonexcitable stem cells have been less explored (26, 49). After evaluating the optoelectronic properties of Si films in the solution (Fig. 4), we examine their influence as exogenous cues on modulating physiological activities of hBMSCs (Figs. 5 and 6). After culturing hBMSCs on Si films with micropillars for 2 hours, we study their electrophysiological activities using the whole-cell patch-clamp recording (Fig. 5A). Under continuous illumination conditions (duration, 3 s), the Si film elicits rapid increases of cell membrane potential, causing cell depolarization (Fig. 5B). At intensities between 0.2 and 1.0 W/cm^2, the cell membrane potential increases by around 3 to 12 mV and reaches its maximum at 0.8 to 1.0 W/cm^2 (Fig. 5C). Depolarizing
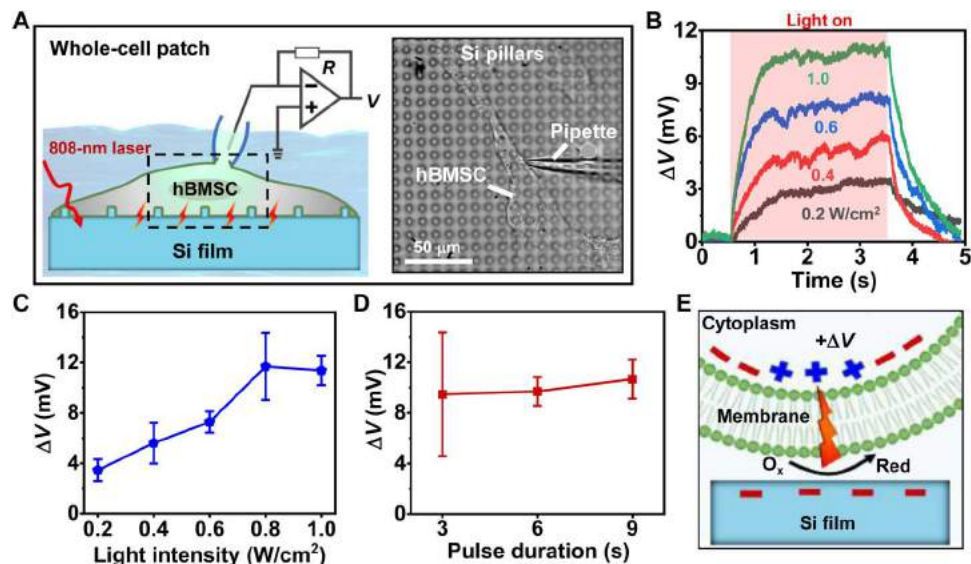
Fig. 5. Photo-induced electrophysiological activities of hBMSCs cultured on Si thin films with pillar structures. (**A**) Left: Scheme of the setup to record cell membrane potentials of hBMSCs with the whole-cell patch model. Right: Optical microscopic image of hBMSCs cultured on Si pillars during patch-clamp recordings. (**B**) Photoinduced membrane voltage changes (ΔV) for hBMSCs on Si samples under illumination with different intensities (duration 3 s). (**C**) Statistics of ΔV versus pulse durations ($n = 5$ cells). (**D**) Statistics of ΔV versus light intensities ($n = 3$ cells). (**E**) Schematic of photoelectric depolarization for hBMSCs.

these hBMSCs does not elicit action potentials (spikes) that are commonly observed in excitable cells such as neurons (*50*). Furthermore, prolonged illumination times are unable to induce additional boost of the membrane potential (Fig. 5D). We exclude the photothermal effects as the temperature rises $\Delta T < 1°C$ under a relatively low irradiation intensity (<1 W/cm^2) in this electrophysiological test (fig. S9). The light-induced cell depolarization can be attributed to the ROS generation caused by the photoelectrochemical process at the Si/cell interface (Fig. 5E). To further understand the results, we establish a circuit model to simulate the Si/cell interaction (fig. S10) (*39, 51, 52*). In the simulation, the Si/cell interface is modeled by a faradaic impedance ($Z_{faradaic}$). A photogenerated voltage increases the membrane voltage, which is in accordance with the experimentally observed cell depolarization.

Correlating with electrophysiological signals, intracellular calcium (Ca^{2+}) activities also reflect important cellular behaviors and are crucial in the osteogenic process by serving as a second messenger (*53*). Conventionally, tethered electrical stimulators have been used to alter Ca^{2+} dynamics and motivate stem cells toward osteogenic differentiation (*54*). Here, we observe the dynamic change of intracellular Ca^{2+} concentration induced by optoelectronic stimulations of Si films under a confocal microscope, by loading hBMSCs with a Ca^{2+} indicator (Fluo-4 AM, green fluorescence) (Fig. 6A). Figure 6B plots representative Ca^{2+} dynamic signals ($\Delta F/F_0$) recorded for a group of hBMSCs cultured on Si. Upon illumination (intensity, 1.0 W/cm^2; duration, 8 s), these cells experience a rapid ascent in Ca^{2+} levels, followed by a slow decline, with fluorescent images before and after illumination provided as insets. As a comparison, hBMSCs cultured on glass yield no Ca^{2+} spikes under similar irradiation (2 W/cm^2 for 10 s), precluding the potential photothermal effects of the 808-nm laser (fig. S11). Further studies show that the peaks of Ca^{2+} levels increase when enhancing the illumination intensity (Fig. 6, C and D) or the pulse duration (Fig. 6, E and F). Last, treatment with *O,O′*-bis(2-

aminophenyl) ethyleneglycol-*N,N,N′,N′*-tetraacetic acid, tetraacetoxymethyl ester (BAPTA-AM), an intracellular calcium chelator (*55*), substantially declines the Ca^{2+} fluorescence (Fig. 6G). These photoinduced Ca^{2+} activities likely originate from the organelle release, which is similar to previously reported cell behaviors triggered by external electrical stimulation (*56*). It is noted that hBMSCs from different batches could have varied activities, which affect the absolute values of fluorescence changes ($\Delta F/F_0$) collected in Fig. 6 (B to G). Despite this fact, the Si microstructure can deterministically modulate instantaneous activities of hBMSCs remotely by light, offering opportunities to regulate their proliferation and differentiation behaviors in a longer time frame.

Regulation of proliferation and osteogenic differentiation for hBMSCs with optoelectronic stimulations in vitro
Results mentioned above demonstrate that optoelectronic signals established by Si microstructures evidently modulate electrophysiological and Ca^{2+} activities of hBMSCs, which are of critical relevance to cells′ long-term behaviors. In Fig. 7, we further culture hBMSCs on Si microstructures for multiple days, investigating cell proliferation and differentiation under optical stimulations. We first evaluate cell viability with the live/dead assay. After being cultured for 7, 14, and 21 days, hBMSCs grow and proliferate normally on Si microstructures both with (Fig. 7A) and without (fig. S12) photo-induced electrical stimulation, indicating ideal biocompatibility of our Si films. Figure 7 (B to E) presents results of ALP and ARS staining performed for hBMSCs cultured on patterned Si films with and without light stimulation (808 nm, 200 mW/cm^2, 3-s duration, 0.2 Hz, 20 min for every other day). After 7-day culture, the ALP production of hBMSCs is substantially enhanced by optoelectronic stimulation (Fig. 7, B and C). In addition to ALP results, ARS staining present a similar light-induced increase in the formation of calcium nodules, indicating a boost of calcium production (Fig. 7, D and E). We also conduct the real-time polymerase chain
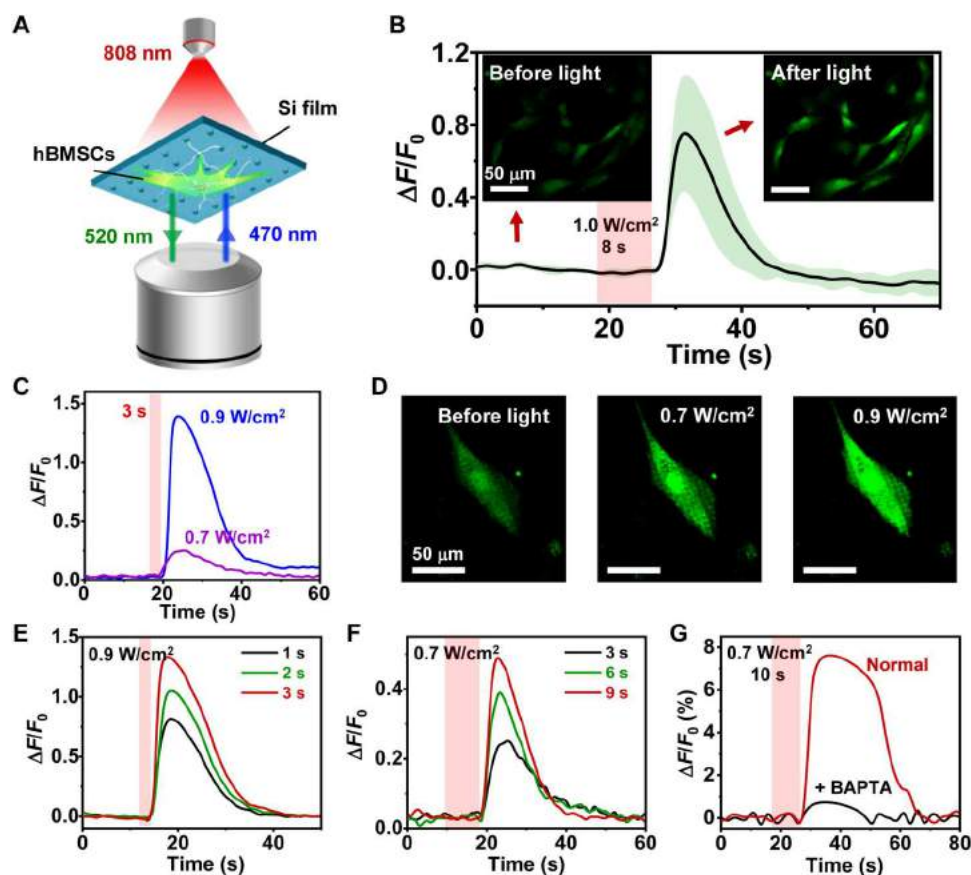
Fig. 6. Photo-induced intracellular calcium (Ca^{2+}) dynamics of hBMSCs cultured on Si films with pillar structures. (**A**) Scheme of the setup for imaging the Ca^{2+} fluorescence. hBMSCs are cultured on Si and stained with Fluo-4 AM (intracellular Ca^{2+} indicator, with the excitation peak at 470 nm and the emission peak at 520 nm). A confocal microscope records the fluorescence images before and immediately after the excitation by an 808-nm laser. (**B**) Ca^{2+} fluorescence signals ($\Delta F/F_0$) of hBMSCs. The solid line and the shaded area indicate the mean and SEM, respectively ($n = 6$ cells). Inset images show the Ca^{2+} fluorescence before and after the laser stimulation. (**C**) Ca^{2+} signals of a cell in response to illumination with different intensities (duration, 3 s). (**D**) Fluorescent images of a cell on Si pillars before and after illumination. (**E** and **F**) Ca^{2+} signals of a cell in response to different illumination parameters. (E) 0.9 W/cm^2 for 1, 2, and 3 s. (F) 0.7 W/cm^2 for 3, 6, and 9 s. (**G**) Comparison of Ca^{2+} signals for cells with and without applying BAPTA as an intracellular calcium chelator.

reaction (PCR) assay to understand the interplay between hBMSCs and optical stimulation at the genetic level. Specifically, ALPP (ALP, placental) reveals the early osteoblastic phenotypic expression during osteogenic differentiation (*57*), SPP1 (secreted phosphoprotein 1) is a mineralized bone matrix protein with high affinity to bind hydroxyapatite during bone remodeling (*58*), and RunX2 (Runt-related transcription factor 2) is a crucial transcription factor regulating numerous related osteogenic genes (*59*). As shown in Fig. 7F, expression levels of ALPP, SPP1, and RunX2 at day 7 are enhanced for hBMSCs experiencing the optoelectronic stimulation, indicating the accelerated osteogenesis. Furthermore, staining results with Cell Counting Kit-8 (CCK-8) suggest that the cell proliferation is also promoted after a 7-day modulation (Fig. 7G). Although these analyses are performed directly on Si films without the 3D scaffold, they provide instructive insights to understand the cell behaviors under optoelectronic stimulations.

In vivo evaluation of bone regeneration with Si-based 3D scaffolds

Leveraging the optoelectronic stimulation effects via Si microstructures, we apply the 3D biomimetic scaffold for bone regeneration in vivo (Fig. 8). Presented in Fig. 8 (A and B), bone defects (~5 mm in diameter) are created in the calvarium of rats. Synthesized mineralized scaffolds incorporating the patterned Si film (Fig. 2A) are implanted into the defect site at both sides, and an 808-nm laser beam is incident on one side for stimulation. The applied illumination conditions are as follows: power, ~0.8 W/cm^2; pulse width, 3 s; frequency, 0.2 Hz; duration, ~20 min every other day for the first 20 days after implantation. The wavelength of 808 nm is within the biological transparency window and enables the remote power transfer to the scaffold underneath the scalp (*60*). Measured and simulated optical transmittance data show that ~30% of the incident intensity can penetrate through a sample of murine skin with a thickness of ~2 mm and enter the skull region, providing sufficient power for optoelectronic stimulations (fig. S13). Furthermore, we assess the biological safety of the radiated IR light, and the beam power of ~0.8 W/cm^2 generates a maximum temperature rise of tissue less than 1.5°C, which is well below the safety limit for body temperatures (*61*, *62*) and minimizes unwanted photothermal effects and potential tissue damages due to overheating (fig. S14). After implanting the scaffolds for a certain period, bone samples are respectively retrieved from rats and undergo radiological and
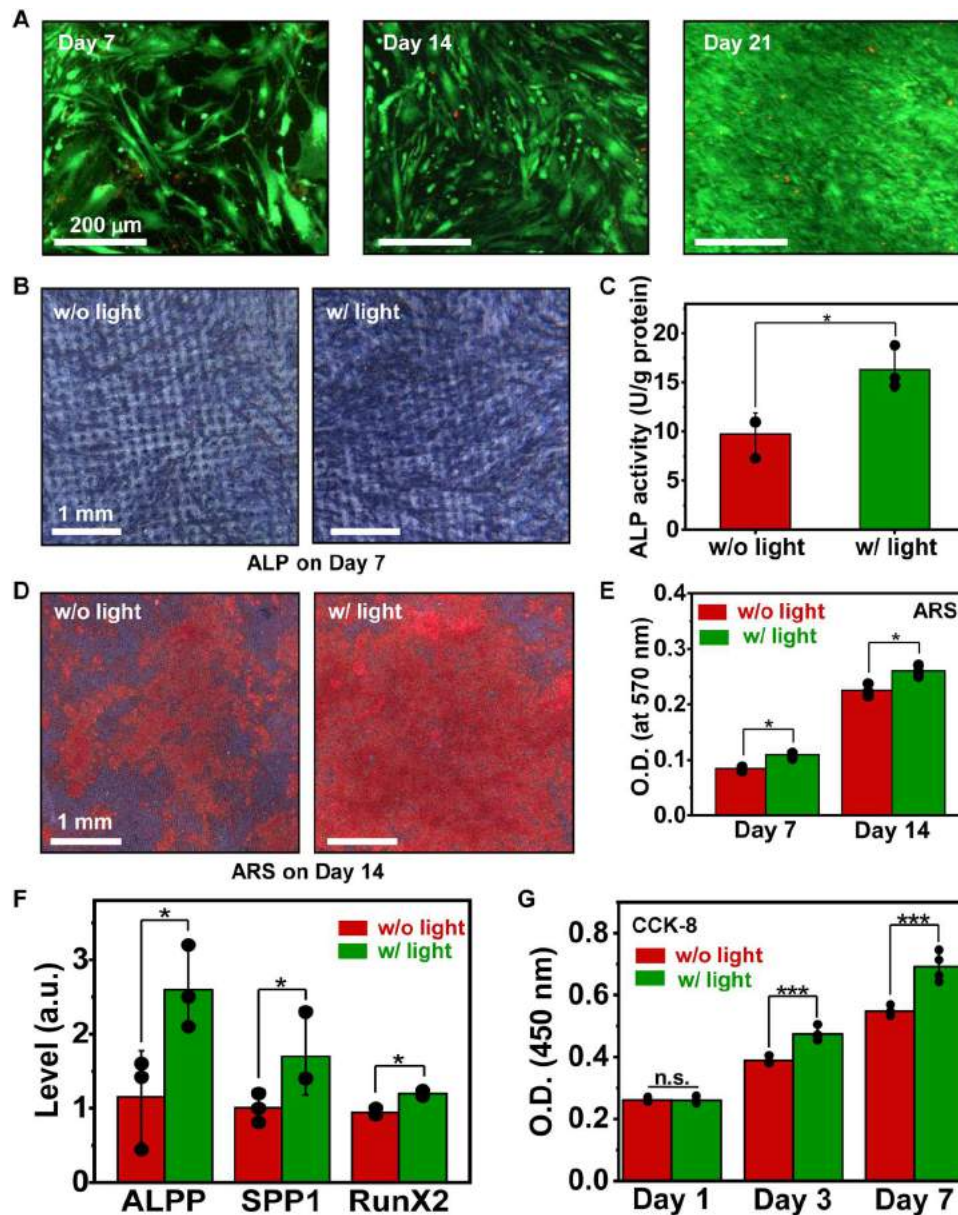
Fig. 7. Osteogenic and proliferation behaviors for hBMSCs on Si structures under endogenous optoelectronic stimulation. (**A**) Fluorescent images showing the chronic biocompatibility of Si pillars, examined by conducting cell live (green)/dead (red) staining tests. (**B**) Coloration and (**C**) quantitative analysis of ALP activities for hBMSCs cultured on Si pillars in the osteogenic induction medium, with and without light (intensity, 200 mW/cm^2; 0.2 Hz; 3 s duration; 20 min every other day for 7 days). (**D**) ARS staining and (**E**) quantitative analysis indicating calcium production for hBMSCs on Si pillars after osteogenic induction combined with and without light (200 mW/cm^2, 0.2 Hz, 3 s duration, 20 min every other day for 7 and 14 days). (**F**) Real-time PCR analysis for osteo-specific genes (ALPP, SPP1, and RunX2) (200 mW/cm^2, 3 s duration, 0.2 Hz, 20 min every other day for 7 days). (**G**) Proliferation behaviors of hBMSCs obtained via CCK-8 tests (200 mW/cm^2, 0.2 Hz, 3 s duration, 20 min, five times per day). Student's t test, *$P < 0.05$, ***$P < 0.001$, n.s., $P > 0.05$.

histological analyses. Figure 8C and fig. S15 show x-ray micro–computed tomography (micro-CT) images for the defect sites after treatment for 4 and 8 weeks, respectively. While the blank group (no scaffold) exhibits little new bone formation even 8 weeks after transplantation (fig. S16), the defect sites filled with bio-scaffolds show large volumes of regenerated bone tissue. Compared to the scaffolds without light stimulations, those under illumination present improved performance, in terms of the bone mineral density (BMD) and the bone trabecular volume (BTV). Facilitated

by optoelectronic stimulations, the averaged BMD increases from 0.118 to 0.168 g/cm^3 at 4 weeks and from 0.135 to 0.225 g/cm^3 at 8 weeks (Fig. 8D). Simultaneously, the averaged BTV increases from 4.88 to 7.65 mm^3 and from 10.2 to 13.5 mm^3 for 4- and 8-week healing periods, respectively (Fig. 8E). Furthermore, we perform hematoxylin and eosin (H&E), Masson, and immunohistological stainings to identify the regenerative bone tissue in defects. The H&E staining images indicate that more newly formed bone and tissue regenerate in the experimental group with photo-induced
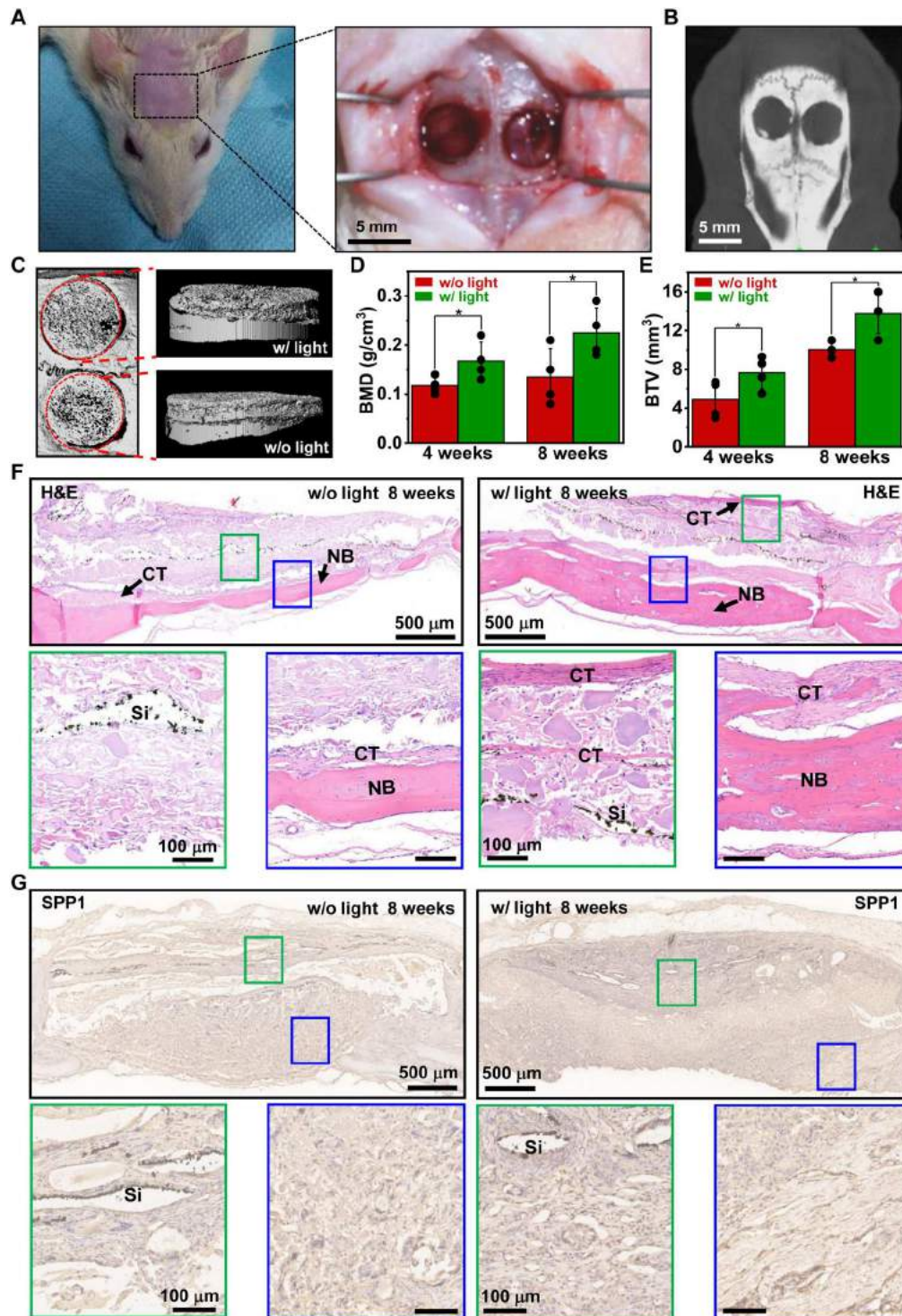
Fig. 8. In vivo evaluation of bone regeneration with Si-based 3D scaffolds. (**A**) Photographs and (**B**) micro-CT image of cranial defects (~5 mm in diameter) generated in a rat model. (**C**) Micro-CT images showing the radiological analysis of bone samples collected 8 weeks after implantation, (left: top view; right: side view). (**D** and **E**) Statistical results of (D) BMD and (E) BTV for newly formed bone tissue. Student's t test, *$P < 0.05$. (**F**) H&E staining and (**G**) immunohistological staining of SPP1 images of regenerated bone tissues with 3D scaffolds 8 weeks after implantation. NB, newly formed bone; CT, connective tissues.

electrical stimulation than that in the control group (without light). Noticeable bulk bone structures form in the middle bottom of the defect cavity 4 weeks after implantation (fig. S17, A and B), and then the new bone nearly covers the whole cranial defect in the experimental group after 8 weeks (Fig. 8F). Moreover, abundant connective fibrous tissues accompanied by dispersive osteoid masses and osteocytes are also clearly observed in all experimental groups. For the immunohistological staining, fig. S17C and Fig. 8G reveal that higher production of SPP1 is expressed in the defect regions after applying optical stimulation, showing deeper brown staining than that of the control group. We also observe higher levels of osteocalcin (OCN; fig. S17D) and collagen type I alpha-1 chain (COL1A1; fig. S17E) expression, especially in the connective tissues near the Si films accompanied with stimulation. It is also known that vascularization always accompanies bone regeneration (63). The influence of our developed scaffold and optical stimulations on the vascularization process requires further investigations. These bone histomorphometrical and histological results demonstrate that the 3D biomimetic scaffolds improve bone regeneration when in synergy with optoelectronic stimulations via Si microstructures.

DISCUSSION

As the most common semiconducting material, Si is widely used as implantable devices for a broad range of biological applications. Currently, most of these devices mainly including transistors and diodes are applied for cellular stimulation (64), recording, and molecular sensing (65). In this work, we introduce an optoelectronic bio-scaffold with thin-film Si-based biointerfaces for bone regeneration. Following the biomimetic design, mineralized and Si materials construct a multiscale hierarchical 3D structure, providing a favorable environment for cell functions. Specifically, the patterned Si film not only promotes cell attachment and growth but also generates electrical stimuli, remotely enabled by IR light, to induce depolarization and enhanced Ca^{2+} activities for hBMSCs. Both in vivo and in vitro experiments demonstrate that the optoelectronic stimulation by Si films can effectively regulate hBMSCs toward osteogenic differentiation and potentiate osteoconductive and osteoinductive properties of scaffolds for bone regeneration. The heterogeneous integrated Si microstructures produce electrical signals controlled by remote IR illumination, eliminating the wired circuitry. In addition, they naturally degrade with the bioscaffold, presenting desirable biocompatibilities. The unique characteristics of sensitive photoresponse, biodegradable Si thin films, and their integration strategies suggest prominent advantages over conventional wired-connected or nondegradable systems.

Advanced Si device design could be envisioned to further improve the optoelectronic response and effectiveness for biological modulations. For instance, Si pn diode structures incorporating coplanar stimulation and return electrodes can be adopted for in vivo optoelectronic stimulations (29, 39, 66). In addition, the current scaffold only has layers of microstructured Si for in vivo demonstration. In the future, the scaffold design can combine more uniformly distributed Si nanomembranes, nanowires, or nanoparticles for improved efficacy. For clinical therapeutics, such optoelectronic stimulation strategies would be constrained by the light penetration in the deep tissue. Applicable scenarios could involve the deployment of these Si-based scaffolds in shallow subdermal bone tissues such

as the skull and articulations. Surface modifications with metallic nanoparticles (30) or nanoporous structures (45) can improve optical responses of Si films, thus reducing the required irradiation power for effective stimulations. Additional efforts on the exploration of proper stimulation patterns (power, duration, frequency, pulse width, etc.) should be performed to realize the optimal bone regeneration. To summarize, results in this study imply that Si-based optoelectronic materials are promising candidates for therapeutics and regenerative medicine.

MATERIALS AND METHODS

Fabrication of the Si-based 3D bio-scaffold

The fabrication process includes the preparation of hierarchical Si mesh and mineralized collagen-based composite (fig. S1). The fabrication of thin-film Si mesh structures starts with silicon-on-insulator substrates (top device layer: 5 μm in thickness; p-type boron doping concentration, ~10^{15} cm^{-3}; resistivity, 1 to 10 ohm·cm; 100 orientation; Soitec, France). Arrays of Si micropillars (height, 2 to 3 μm; diameter, 2 μm; pitch, 10 μm) are prepared by using photolithographic process and dry etching. Wet etching in the potassium hydroxide solution (2 mg/10 ml, 80°C, 5 to 10 min) defines the random nanosized pyramids (~200 nm in height). The patterned mesh structures (hole size, 200 × 200 μm^2; pitch, 200 μm) are fabricated by a photolithographic and dry-etching process. Last, freestanding, thin-film Si meshes are retrieved by removing the silicon dioxide sacrificial layer in a hydrofluoric acid solution. Poly(dimethylsiloxane) stamps pick up released thin-film Si meshes and transfer them into the bottom of a customized Teflon cylindrical mold (thickness, ~0.8 mm; diameter, 5 to 6 mm). The synthesis of mineralized collagen/PCL scaffold has been described in previous work (13). First, powders of HA-mineralized collagen and the PCL (molecular weight, 300,000) are added into the 1,4-dioxane solvent in a solid/liquid ratio of 1:1:10 (g/ml). After 4 hours of magnetic stirring, a homogeneous slurry forms. The rheological properties of the slurry are characterized via a rheometer (Anton Paar Physica MCR 301/302), as shown in fig. S18, demonstrating the easy molding of the slurry. The collagen/PCL slurry is subsequently poured into the cylindrical mold with the thin-film Si mesh in the bottom. After being stored at −20°C overnight, a lyophilization process removes the organic solvent and creates the hybrid scaffold.

Optoelectronic characterizations of Si films

A patch-clamp setup is used to measure the photon response properties of the Si thin films in 1× PBS solution (pH 7.4). A laser beam (808 nm, ~4 mm spot size) is normally incident on the surfaces of Si samples and controlled by transistor-transistor logic signals. A pipette electrode (~500 kilohms) filled with PBS is positioned close to (3 to 5 μm) the tested sample (Si thin films or scaffolds) surface. Voltage- and current-clamp recordings are performed with an Axopatch 200B amplifier controlled by pClamp software (Molecular Devices). The photocurrent signals are collected with the voltage-clamp recording model under illumination (frequency, 1 Hz; pulse duration, 10 ms). The steady-state photovoltage responses are recorded by the current-clamp model under illumination (frequency, 0.2 Hz; pulse duration, 3 s) for the Si thin films grounded by gold as the backside electrode.

ROS detection

The generation of ROS at the Si/solution interface after optical stimulations is detected using the DCFH ROS probe acquired from the commercial DCFH-DA kit (APExBio Technology LLC, USA) and by dissolving it in a sodium hydroxide solution (pH 10). After being placed at room temperature for 20 min, the DCFH probe is diluted with PBS solution, which is adjusted to the neutral level. Si samples are immersed in the solution and illuminated with an 808-nm laser. The fluorescent spectra are collected by a fluorometer (Ex/Em: 488/525 nm).

Electrostatic simulations

The electrical potential distribution for the Si thin film in solution is numerically simulated using a finite element analysis model (COMSOL Multiphysics v5.5) by performing the Electrical Static (EC) module in 2D geometry. The silicon thin film serves as a charged photocapacitor, and the top surface (exposed to solution) is set to equipotential surface with a value of 100 mV. The PBS solution is assumed a dielectric with a relative permittivity of 80. The distance from the boundary of solution to the center of silicon equipotential surface is 2 to 3 cm, and the boundary potential is fixed at 0 V.

Thermal and optical characterizations

The tissue temperature is measured in vitro by inserting a thermocouple (IT-24P, BAT-10R, Physitemp Instruments, LLC) into an isolated rat scalp tissue (insertion depth, ~2 mm), which is illuminated by an 808-nm laser (power, 0.8 W/cm^2; frequency, 0.2 Hz; pulse duration, 3 s). Optical transmission spectra of the scalp tissue and Si films are measured by an ultraviolet–visible–near-IR spectrometer (Cary 5000, Agilent) with an integrating sphere.

Thermal and optical simulations

The simulation is conducted using the "Absorption-Scattering" and "Bioheat-Transfer" coupling multiphysics in COMSOL. The corresponding parameters (density, thermal conductivity, heat capacity, optical absorption, and scattering coefficients at 808 nm) used in the model include the following: skin tissue (1.1 g/cm^3, 0.37 W/m per kelvin, 3.4 J/g per kelvin, 50/m, and 2500/m), bone tissue (1.9 g/cm^3, 1.16 W/m per kelvin, 1.3 J/g per kelvin, 100/m, and 5000/m), and brain tissue (1.1 g/cm^3, 0.5 W/m per kelvin, 3.7 J/g per kelvin, 50/m, and 1200/m). An 808-nm laser beam (power, 800 mW/cm^2; spot size, 5 mm) is set as the heat source. The heat transfer boundary condition for skin (37°C) to air (25°C) is convective heater flux.

Characterization of cellular morphology

Before cell culture, the samples (scaffolds or Si thin films) are pretreated with dopamine solution [dopamine hydrochloride of 2 mg/ml in 10 mM tris-HCl buffer solution (pH 8.5)] for 30 min at room temperature, creating hydrophilic surfaces (fig. S4) for improved cell adhesion. The scaffolds or Si thin-film samples are placed into well plates, with suspensions of hBMSCs (#7500, ScienCell, Carlsbad, CA, USA) or MC3T3-E1 cells dropped onto sample surfaces. Cells are incubated in cell culture media [high-glucose Dulbecco's modified Eagle's medium (DMEM) for hBMSCs and minimum essential medium α (MEMα) for MC3T3-E1 cells], supplemented with 10% fetal bovine serum and 1% penicillin-streptomycin (Thermo Fisher Scientific, Waltham, MA, USA) at 37°C with 5% CO$_2$. Cell morphologies are characterized by an SEM (Zeiss

Merlin) and a fluorescence confocal microscope (LSM710, Zeiss) [green: phalloidin staining actin cytoskeleton; blue: nuclei stained with 4′,6-diamidino-2-phenylindole (DAPI)]. Fluorescence images are analyzed with the ImageJ software.

Characterization of cell migration

MC3T3-E1 cells are seeded on planar Si and Si pillars (~10,000 cells/cm^2), respectively, and cultured for 24 hours in MEMα medium without fetal bovine serum. Gently scraping the cells with a P200 pipette tip creates scratches on Si film surfaces. The scratched surfaces are washed twice with PBS solutions to remove the debris and nonadherent cells. After culturing for another 0, 6, or 24 hours, the phalloidin dye solution is used to stain cells' actin cytoskeleton, and fluorescence images are taken to capture cell migration behaviors at selected time points.

Electrophysiological recording

For whole-cell recordings, pipettes are filled with internal solution containing the following components: 145 mM KCl, 5 mM H-Hepes, 10 mM EGTA, 5 mM adenosine triphosphate–Na, and 5 mM guanosine triphosphate–K. The internal solution was adjusted to pH 7.4 by KOH solution. External solution contains the following components: 150 mM NaCl, 5 mM NaH$_2$PO$_4$, 10 mM H-Hepes, and 10 mM D-glucose, adjusted to pH 7.4 with NaOH solution. Recording electrode's resistance is 3 to 5 megohms pulled with a micropipette puller. The membrane voltages are recorded with a computer-controlled amplifier (HEKA, Harvard Bioscience, Inc.) in the current-clamp mode. The hBMSCs are seeded on Si films for ~2 hours and illuminated by an 808-nm laser with adjustable power intensity, frequency, and duration controlled by a function generator.

Calcium imaging in vitro

hBMSCs are loaded with Fluo-4 AM (Thermo Fisher Scientific; diluted by 1000 times for use) at 37°C for 25 min. After washing three times with PBS, the cells' Ca^{2+} fluorescent signals are imaged with a confocal microscope (LSM710, Zeiss). An 808-nm laser beam is normally incident onto Si samples and controlled by a function generator. To chelate the intracellular Ca^{2+}, BAPTA-AM is added to the culture medium (concentration, 10 μM), and cells are incubated for 40 min before recording the fluorescent signals. The fluorescence images are analyzed via the Zen 2.6 Zeiss software. Normalized fluorescence changes are calculated as $\Delta F/F_0 = (F - F_0)/F_0$, where F_0 is the initial fluorescent intensity before laser illumination.

In vitro proliferation and biocompatibility tests

The hBMSCs are seeded on the surface of Si samples with a density of 4000 cells/cm^2 and cultured in the DMEM. Cell proliferation is analyzed with CCK-8 (Dojindo, Japan). Biocompatibility of Si films (with and without light) is characterized using the live/dead assay kit (KeyGEN, Nanjing, China). Calcein-AM and propidium iodide stain viable (green fluorescent) and dead (red fluorescent) cells, respectively. A fluorescence microscope (Olympus, Japan) takes images of live and dead cells.

In vitro osteogenic evaluation

The cell culture medium for inducing osteogenesis is DMEM containing 10% fetal bovine serum (Gibco), 1% penicillin-streptomycin

(Gibco), 200 μM L-ascorbic acid (Sigma-Aldrich, USA), 10 mM β-glycerophosphate disodium (Sigma-Aldrich), and 100 nM dexamethasone (Sigma-Aldrich). The initial seeding density is ~15,000 cells/cm^2, and the culture medium is replaced every 48 hours. The illumination conditions for hBMSCs on Si microstructures are as follows: 200 mW/cm^2, 0.2 Hz, 3 s duration, and 20 min every other day. ALP and ARS staining are conducted to evaluate the formation of ALP and mineralized nodules. After the osteogenic induction process, cells are firstly fixed in 4% paraformaldehyde for 10 min. After rinsing with PBS, cells are incubated in 1% ARS dye (for ARS) or bromochloroindolyl phosphate/nitro blue tetrazolium ALP Color Development Kit (Beyotime Institute of Biotechnology, China) (for ALP) for 30 min. Last, excess staining solutions are removed with deionized water for staining color observation. Quantitative measurement of ALP activity is performed by an ALP assay kit (Nanjing Jiancheng). For quantitative detection of mineralized nodules, the ARS-stained samples are immersed into 1% hexadecylpyridinium chloride monohydrate (Sigma-Aldrich) for 1 hour, and the absorbance is detected at 550 nm using a microplate reader (BioTek Instruments, USA).

mRNA is extracted from hBMSCs cultured on Si thin films using Trizol (Invitrogen, USA) at day 7. Reverse transcription is carried out using a PrimeScript RT reagent kit (TaKaRa, Japan), and reverse transcription quantitative real-time PCR (RT-qPCR) is conducted on QuantStudio 3 (Thermo Fisher Scientific, USA) with the SYBR green dye (Roche, USA). Glyceraldehyde-3-phosphate dehydrogenase serves as the housekeeping gene. Osteogenic-related factors including ALPP, SPP1, and RUNX2 are detected by RT-qPCR.

In vivo bone regeneration
All procedures involving animals are approved by the Animal Research Committee of Peking Union Medical College Hospital and the Laboratory Animal Center of Peking Union Medical College Hospital, which strictly adhered to the *Guide for the Care and Use of Laboratory Animals* (GB14925-2010; NIH). All animals are socially housed in a 12-hour light/12-hour dark cycle (lights on at 8 a.m.), with food and water ad libitum. Sprague-Dawley rats (male, 6 weeks old, ~300 g) are purchased from VitalRiver (Beijing, China). Animals are anesthetized with 1% pentobarbital sodium by intraperitoneal injection. After exposing the skull through a skin incision and blunt dissection, full thickness cranial defects with critical sizes (5 mm in diameter) are created by a cylindrical drill under cooling conditions with saline water. Then, the hybrid scaffolds are implanted into the defects. The optical stimulations are performed every other day (0.8 W/cm^2, 0.2 Hz, 3 s duration, 20 min each time). Animals are euthanized 8 weeks after surgery, and cranial tissues with defects are fixed in paraformaldehyde solution. Then, the samples are scanned by a micro-CT system (Skyscan, 1172, Bruker), together with 3D reconstruction and quantitative analysis of bone regeneration via the supporting analysis software (CTAn, CTVol, CTVox, and Data Viewer). A standard bone material is used to calibrate the system for BMD and BTV analysis. After EDTA (Thermo Fisher Scientific) treatment and gradient alcohol dehydration, H&E, Masson, SPP1 (1:1000 dilution; Servicebio, China), OCN (1:300 dilution; Servicebio, China), and COL1A1 (1:200 dilution; Solarbio, China) staining are conducted on the tissues via standard procedures.

Supplementary Materials
This PDF file includes:
Figs. S1 to S18

REFERENCES AND NOTES

1. GBD 2019 Fracture Collaborators, Global, regional, and national burden of bone fractures in 204 countries and territories, 1990-2019: A systematic analysis from the Global Burden of Disease Study 2019. *Lancet Healthy Longev.* **2**, e580–e592 (2021).

2. F. Borgstrom, L. Karlsson, G. Ortsater, N. Norton, P. Halbout, C. Cooper, M. Lorentzon, E. V. McCloskey, N. C. Harvey, M. K. Javaid, J. A. Kanis; International Osteoporosis Foundation, Fragility fractures in Europe: Burden, management and opportunities. *Arch. Osteoporos.* **15**, 59 (2020).

3. C. Pike, H. G. Birnbaum, M. Schiller, H. Sharma, R. Burge, E. T. Edgell, Direct and indirect costs of non-vertebral fracture patients with osteoporosis in the US. *Pharmacoeconomics* **28**, 395–409 (2010).

4. A. G. Mikos, S. W. Herring, P. Ochareon, J. Elisseeff, H. H. Lu, R. Kandel, F. J. Schoen, M. Toner, D. Mooney, A. Atala, M. E. Van Dyke, D. Kaplan, G. Vunjak-Novakovic, Engineering complex tissues. *Tissue Eng.* **12**, 3307–3339 (2006).

5. K. Sadtler, A. Singh, M. T. Wolf, X. K. Wang, D. M. Pardoll, J. H. Elisseeff, Design, clinical translation and immunological response of biomaterials in regenerative medicine. *Nat. Rev. Mater.* **1**, 16040 (2016).

6. A. M. McDermott, S. Herberg, D. E. Mason, J. M. Collins, H. B. Pearson, J. H. Dawahare, R. Tang, A. N. Patwa, M. W. Grinstaff, D. J. Kelly, E. Alsberg, J. D. Boerckel, Recapitulating bone development through engineered mesenchymal condensations and mechanical cues for tissue regeneration. *Sci. Transl. Med.* **11**, 495 (2019).

7. A. Khademhosseini, R. Langer, A decade of progress in tissue engineering. *Nat. Protoc.* **11**, 1775–1781 (2016).

8. A. K. Gaharwar, I. Singh, A. Khademhosseini, Engineered biomaterials for in situ tissue regeneration. *Nat. Rev. Mater.* **5**, 686–705 (2020).

9. J. An, J. E. M. Teoh, R. Suntornnond, C. K. Chua, Design and 3D printing of scaffolds and tissues. *Engineering* **1**, 261–268 (2015).

10. G. L. Koons, M. Diba, A. G. Mikos, Materials design for bone-tissue engineering. *Nat. Rev. Mater.* **5**, 584–603 (2020).

11. Y. Y. Du, J. L. Guo, J. L. Wang, A. G. Mikos, S. M. Zhang, Hierarchically designed bone scaffolds: From internal cues to external stimuli. *Biomaterials* **218**, 119334 (2019).

12. A. Haider, S. Haider, S. S. Han, I. K. Kang, Recent advances in the synthesis, functionalization and biomedical applications of hydroxyapatite: A review. *RSC Adv.* **7**, 7442–7458 (2017).

13. S. Wang, Y. D. Yang, G. L. Koons, A. G. Mikos, Z. Y. Qiu, T. X. Song, F. Z. Cui, X. M. Wang, Tuning pore features of mineralized collagen/PCL scaffolds for cranial bone regeneration in a rat model. *Mater. Sci. Eng. C Mater. Biol. Appl.* **106**, 110186 (2020).

14. H. Zhou, J. Lee, Nanoscale hydroxyapatite particles for bone tissue engineering. *Acta Biomater.* **7**, 2769–2781 (2011).

15. L. Yu, D. W. Rowe, I. P. Perera, J. Y. Zhang, S. L. Suib, X. N. Xin, M. Wei, Intrafibrillar mineralized collagen–hydroxyapatite-based scaffolds for bone regeneration. *ACS Appl. Mater. Interfaces* **12**, 18235–18249 (2020).

16. G. L. Koons, A. G. Mikos, Progress in three-dimensional printing with growth factors. *J. Control. Release* **295**, 50–59 (2019).

17. H. C. Wang, P. C. Sun, L. Yin, X. Sheng, 3D electronic and photonic structures as active biological interfaces. *Infomat.* **2**, 527–552 (2020).

18. L. Wang, C. F. Lu, S. H. Yang, P. C. Sun, Y. Wang, Y. J. Guan, S. Liu, D. L. Cheng, H. Y. Meng, Q. Wang, J. G. He, H. Q. Hou, H. Li, W. Lu, Y. X. Zhao, J. Wang, Y. Q. Zhu, Y. X. Li, D. Luo, T. Li, H. Chen, S. R. Wang, X. Sheng, W. Xiong, X. M. Wang, J. Peng, L. Yin, A fully biodegradable and self-electrified device for neuroregenerative medicine. *Sci. Adv.* **6**, eabc6686 (2020).

19. L. Z. Li, L. H. Lu, Y. Q. Ren, G. Tang, Y. Zhao, X. Cai, Z. Shi, H. Ding, C. B. Liu, D. L. Cheng, Y. Xie, H. C. Wang, X. Fu, L. Yin, M. M. Luo, X. Sheng, Colocalized, bidirectional optogenetic modulations in freely behaving mice with a wireless dual-color optoelectronic probe. *Nat. Commun.* **13**, 839 (2022).

20. C. Goldstein, S. Sprague, B. A. Petrisor, Electrical stimulation for fracture healing: Current evidence. *J. Orthop. Trauma* **24**, S62–S65 (2010).

21. G. Thrivikraman, S. K. Boda, B. Basu, Unraveling the mechanistic effects of electric field stimulation towards directing stem cell fate and function: A tissue engineering perspective. *Biomaterials* **150**, 60–86 (2018).

22. X. Huang, L. Wang, H. Wang, B. Zhang, X. Wang, R. Y. Z. Stening, X. Sheng, L. Yin, Materials strategies and device architectures of emerging power supply devices for implantable bioelectronics. *Small* **16**, e1902827 (2020).

23. D. Rand, M. Jakesova, G. Lubin, I. Vebraite, M. David-Pur, V. Đerek, T. Cramer, N. S. Sariciftci, Y. Hanein, E. D. Glowacki, Direct electrical neurostimulation with organic pigment photocapacitors. *Adv. Mater.* **30**, 1707292 (2018).

24. C. Y. Ning, P. Yu, Y. Zhu, M. Y. Yao, X. J. Zhu, X. L. Wang, Z. F. Lin, W. P. Li, S. Y. Wang, G. X. Tan, Y. Zhang, Y. J. Wang, C. B. Mao, Built-in microscale electrostatic fields induced by anatase–rutile-phase transition in selective areas promote osteogenesis. *NPG Asia Mater.* **8**, e243 (2016).

25. J. Tian, R. Shi, Z. Liu, H. Ouyang, M. Yu, C. Zhao, Y. Zou, D. Jiang, J. Zhang, Z. Li, Self-powered implantable electrical stimulator for osteoblasts' proliferation and differentiation. *Nano Energy* **59**, 705–714 (2019).

26. M. Jakesova, M. S. Ejneby, V. Đerek, T. Schmidt, M. Gryszel, J. Brask, R. Schindl, D. T. Simon, M. Berggren, F. Elinder, E. D. Glowacki, Optoelectronic control of single cells using organic photocapacitors. *Sci. Adv.* **5**, eaav5265 (2019).

27. F. Lodola, N. Martino, G. Tullii, G. Lanzani, M. R. Antognazza, Conjugated polymers mediate effective activation of the mammalian ion channel transient receptor potential vanilloid 1. *Sci. Rep.* **7**, 8477 (2017).

28. M. Leccardi, N. A. L. Chenais, L. Ferlauto, M. Kawecki, E. G. Zollinger, D. Ghezzi, Photovoltaic organic interface for neuronal stimulation in the near-infrared. *Commun. Mater.* **1**, 21 (2020).

29. M. S. Ejneby, M. Jakesova, J. J. Ferrero, L. Migliaccio, I. Sahalianov, Z. F. Zhao, M. Berggren, D. Khodagholy, V. Đerek, J. N. Gelinas, E. D. Glowacki, Chronic electrical stimulation of peripheral nerves via deep-red light transduced by an implanted organic photocapacitor. *Nat. Biomed. Eng.* **6**, 741–753 (2022).

30. Y. Jiang, X. Li, B. Liu, J. Yi, Y. Fang, F. Shi, X. Gao, E. Sudzilovsky, R. Parameswaran, K. Koehler, V. Nair, J. Yue, K. H. Guo, Y. Fang, H.-M. Tsai, G. Freyermuth, R. C. S. Wong, C.-M. Kao, C.-T. Chen, A. W. Nicholls, X. Wu, G. M. G. Shepherd, B. Tian, Rational design of silicon structures for optically controlled multiscale biointerfaces. *Nat. Biomed. Eng.* **2**, 508–521 (2018).

31. L. L. Wang, K. Mathieson, T. I. Kamins, J. D. Loudin, L. Galambos, G. Goetz, A. Sher, Y. Mandel, P. Huie, D. Lavinsky, J. S. Harris, D. V. Palanker, Photovoltaic retinal prosthesis: Implant fabrication and performance. *J. Neural Eng.* **9**, 046014 (2012).

32. F. Lodola, V. Rosti, G. Tullii, A. Desii, L. Tapella, P. Catarsi, D. Lim, F. Moccia, M. R. Antognazza, Conjugated polymers optically regulate the fate of endothelial colony-forming cells. *Sci. Adv.* **5**, eaav4620 (2019).

33. F. J. O'Brien, Biomaterials & scaffolds for tissue engineering. *Mater. Today* **14**, 88–95 (2011).

34. X. Sheng, J. Liu, I. Kozinsky, A. M. Agarwal, J. Michel, L. C. Kimerling, Design and non-lithographic fabrication of light trapping structures for thin film silicon solar cells. *Adv. Mater.* **23**, 843–847 (2011).

35. C. Xu, S. Yu, W. Wu, Q. Liu, L. Ren, Direct ink writing of Fe bone implants with independently adjustable structural porosity and mechanical properties. *Addit. Manuf.* **51**, 102589 (2022).

36. L. Wang, Y. Gao, F. Dai, D. Kong, H. Wang, P. Sun, Z. Shi, X. Sheng, B. Xu, L. Yin, Geometrical and chemical-dependent hydrolysis mechanisms of silicon nanomembranes for biodegradable electronics. *ACS Appl. Mater. Interfaces* **11**, 18013–18023 (2019).

37. C. M. Li, C. C. Guo, V. Fitzpatrick, A. Ibrahim, M. J. Zwierstra, P. Hanna, A. Lechtig, A. Nazarian, S. J. Lin, D. L. Kaplan, Design of biodegradable, implantable devices towards clinical translation. *Nat. Rev. Mater.* **5**, 61–81 (2020).

38. M. A. Woodruff, D. W. Hutmacher, The return of a forgotten polymer—Polycaprolactone in the 21st century. *Prog. Polym. Sci.* **35**, 1217–1256 (2010).

39. Y. X. Huang, Y. T. Cui, H. J. Deng, J. J. Wang, R. Q. Hong, S. H. Hu, H. Q. Hou, Y. R. Dong, H. C. Wang, J. Y. Chen, L. Z. Li, Y. Xie, P. C. Sun, X. Fu, L. Yin, W. Xiong, S. H. Shi, M. M. Luo, S. R. Wang, X. J. Li, X. Sheng, Bioresorbable thin-film silicon diodes for the optoelectronic excitation and inhibition of neural activities. *Nat. Biomed. Eng.* 10.1038/s41551-022-00931-0 , (2022).

40. S. Pina, J. M. Oliveira, R. L. Reis, Natural-based nanocomposites for bone tissue engineering and regenerative medicine: A review. *Adv. Mater.* **27**, 1143–1169 (2015).

41. S. G. Higgins, M. Becce, A. Belessiotis-Richards, H. Seong, J. E. Sero, M. M. Stevens, High-aspect-ratio nanostructured surfaces as biological metamaterials. *Adv. Mater.* **32**, 1903862 (2020).

42. C. S. Hansel, S. W. Crowder, S. Cooper, S. Gopal, M. J. P. da Cruz, L. D. Martins, D. Keller, S. Rothery, M. Becce, A. E. G. Cass, C. Bakal, C. Chiappini, M. M. Stevens, Nanoneedle-mediated stimulation of cell mechanotransduction machinery. *ACS Nano* **13**, 2913–2926 (2019).

43. H. C. Wang, J. J. Tian, B. W. Lu, Y. Xie, P. C. Sun, L. Yin, Y. G. Wang, X. Sheng, Degradation study of thin-film silicon structures in a cell culture medium. *Sensors* **22**, 802 (2022).

44. S.-W. Hwang, G. Park, C. Edwards, E. A. Corbin, S.-K. Kang, H. Cheng, J.-K. Song, J.-H. Kim, S. Yu, J. Ng, J. E. Lee, J. Kim, C. Yee, B. Bhaduri, Y. Su, F. G. Omenetto, Y. Huang, R. Bashir, L. Goddard, G. Popescu, K.-M. Lee, J. A. Rogers, Dissolution chemistry and biocompatibility of single-crystalline silicon nanomembranes and associated materials for transient electronics. *ACS Nano* **8**, 5843–5851 (2014).

45. A. Prominski, J. Shi, P. Li, J. Yue, Y. Lin, J. Park, B. Tian, M. Y. Rotenberg, Porosity-based heterojunctions enable leadless optoelectronic modulation of tissues. *Nat. Mater.* **21**, 647–655 (2022).

46. F. Moccia, S. Negri, P. Faris, C. Ronchi, F. Lodola, Optical excitation of organic semiconductors as a highly selective strategy to induce vascular regeneration and tissue repair. *Vascul. Pharmacol.* **144**, 106998 (2022).

47. M. R. Antognazza, I. Abdel Aziz, F. Lodola, Use of exogenous and endogenous photomediators as efficient ROS modulation tools: Results and perspectives for therapeutic purposes. *Oxid. Med. Cell. Longev.* **2019**, 2867516 (2019).

48. M. Levin, Morphogenetic fields in embryogenesis, regeneration, and cancer: Non-local control of complex patterning. *Biosystems* **109**, 243–261 (2012).

49. S. Sundelacruz, A. T. Moody, M. Levin, D. L. Kaplan, Membrane potential depolarization alters calcium flux and phosphate signaling during osteogenic differentiation of human mesenchymal stem cells. *Bioelectricity* **1**, 56–66 (2019).

50. X. Duan, T.-M. Fu, J. Liu, C. M. Lieber, Nanoelectronics-biology frontier: From nanoscopic probes for action potential recording in live cells to three-dimensional cyborg tissues. *Nano Today* **8**, 351–373 (2013).

51. I. Schoen, P. Fromherz, The mechanism of extracellular stimulation of nerve cells on an electrolyte-oxide-semiconductor capacitor. *Biophys. J.* **92**, 1096–1111 (2007).

52. A. Mariano, C. Lubrano, U. Bruno, C. Ausilio, N. B. Dinger, F. Santoro, Advances in cell-conductive polymer biointerfaces and role of the plasma membrane. *Chem. Rev.* **122**, 4552–4580 (2022).

53. M. N. Lee, H. S. Hwang, S. H. Oh, A. Roshanzadeh, J. W. Kim, J. H. Song, E. S. Kim, J. T. Koh, Elevated extracellular calcium ions promote proliferation and migration of mesenchymal stem cells via increasing osteopontin expression. *Exp. Mol. Med.* **50**, 1–16 (2018).

54. M. R. Love, S. Palee, S. C. Chattipakorn, N. Chattipakorn, Effects of electrical stimulation on cell proliferation and apoptosis. *J. Cell. Physiol.* **233**, 1860–1876 (2018).

55. S. Li, D. Lu, J. Tang, J. Min, M. Hu, Y. Li, Y. Liu, L. Wang, C. Liu, L. Hong, Electrical stimulation activates fibroblasts through the elevation of intracellular free Ca^{2+}: Potential mechanism of pelvic electrical stimulation therapy. *Biomed. Res. Int.* **2019**, 7387803 (2019).

56. S. Sun, Y. Liu, S. Lipsky, M. Cho, Physical manipulation of calcium oscillations facilitates osteodifferentiation of human mesenchymal stem cells. *FASEB J.* **21**, 1472–1480 (2007).

57. S. Vimalraj, Alkaline phosphatase: Structure, expression and its function in bone mineralization. *Gene* **754**, 144855 (2020).

58. P. Lekic, J. Sodek, C. A. G. McCulloch, Relationship of cellular proliferation to expression of osteopontin and bone sialoprotein in regenerating rat periodontium. *Cell Tissue Res.* **285**, 491–500 (1996).

59. L. D. Carbonare, G. Innamorati, M. T. Valenti, Transcription factor Runx2 and its application to bone tissue engineering. *Stem Cell Rev. Rep.* **8**, 891–897 (2012).

60. E. Moon, D. Blaauw, J. D. Phillips, Subcutaneous photovoltaic infrared energy harvesting for bio-implantable devices. *IEEE Trans. Electron Devices* **64**, 2432–2437 (2017).

61. A. Bozkurt, B. Onaral, Safety assessment of near infrared light emitting diodes for diffuse optical measurements. *Biomed. Eng. Online* **3**, 9 (2004).

62. M. Nourhashemi, M. Mahmoudzadeh, F. Wallois, Thermal impact of near-infrared laser in advanced noninvasive optical brain imaging. *Neurophotonics* **3**, 015001 (2016).

63. G. Y. Wang, N. Yuan, N. Y. Li, Q. J. Wei, Y. P. Qian, J. Zhang, M. Qin, Y. G. Wang, S. W. Dong, Vascular endothelial growth factor mimetic peptide and parathyroid hormone (1–34) delivered via a blue-light-curable hydrogel synergistically accelerate bone regeneration. *ACS Appl. Mater. Interfaces* **14**, 35319–35332 (2022).

64. R. Parameswaran, J. L. Carvalho-de-Souza, Y. Jiang, M. J. Burke, J. F. Zimmerman, K. Koehler, A. W. Phillips, J. Yi, E. J. Adams, F. Bezanilla, B. Tian, Photoelectrochemical modulation of neuronal activity with free-standing coaxial silicon nanowires. *Nat. Nanotechnol.* **13**, 260–266 (2018).

65. S.-K. Kang, R. K. Murphy, S.-W. Hwang, S. M. Lee, D. V. Harburg, N. A. Krueger, J. Shin, P. Gamble, H. Cheng, S. Yu, Z. Liu, J. G. McCall, M. Stephen, H. Ying, J. Kim, G. Park, R. C. Webb, C. H. Lee, S. Chung, D. S. Wie, A. D. Gujar, B. Vemulapalli, A. H. Kim, K.-M. Lee, J. Cheng, Y. Huang, S. H. Lee, P. V. Braun, W. Z. Ray, J. A. Rogers, Bioresorbable silicon electronic sensors for the brain. *Nature* **530**, 71–76 (2016).

66. K. Mathieson, J. Loudin, G. Goetz, P. Huie, L. L. Wang, T. I. Kamins, L. Galambos, R. Smith, J. S. Harris, A. Sher, D. Palanker, Photovoltaic retinal prosthesis with high pixel density. *Nat. Photonics* **6**, 391–397 (2012).

Acknowledgments

Science Advances

A 3D biomimetic optoelectronic scaffold repairs cranial defects

Huachun Wang, Jingjing Tian, Yuxi Jiang, Shuang Liu, Jingchuan Zheng, Ningyu Li, Guiyan Wang, Fan Dong, Junyu Chen, Yang Xie, Yunxiang Huang, Xue Cai, Xiumei Wang, Wei Xiong, Hui Qi, Lan Yin, Yuguang Wang, and Xing Sheng

View the article online
https://www.science.org/doi/10.1126/sciadv.abq7750
Permissions
https://www.science.org/help/reprints-and-permissions

Use of this article is subject to the Terms of service

Science Advances

▉AAAS

Supplementary Materials for

A 3D biomimetic optoelectronic scaffold repairs cranial defects

Huachun Wang *et al.*

Corresponding author: Yuguang Wang, wangyuguang@bjmu.edu.cn; Xing Sheng, xingsheng@tsinghua.edu.cn

This PDF file includes:

Figs. S1 to S18

Fig. S1.
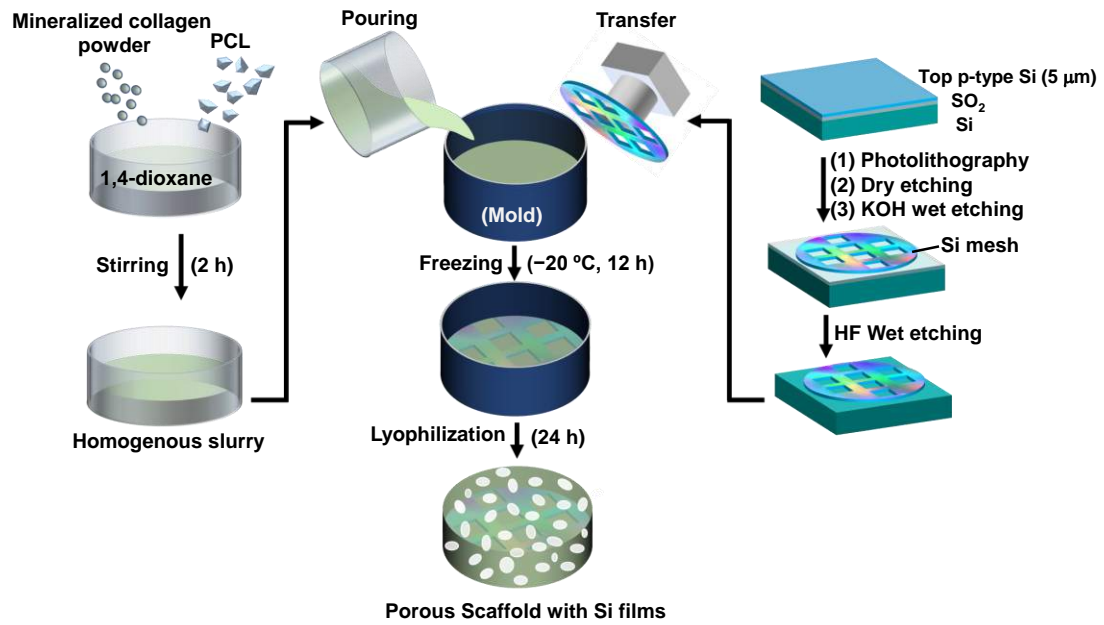
Fig. S1. Schematic illustration of processing flow for the fabrication of Si based 3D optoelectronic scaffold.

Fig. S2.
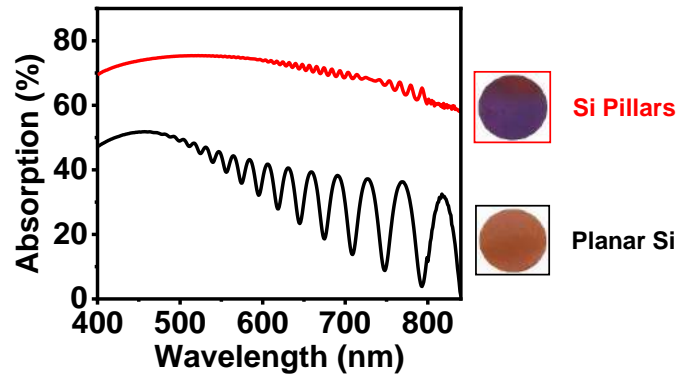
Fig. S2. Optical images and corresponding absorption spectra for Si pillars and planar Si samples.

Fig. S3.

A

Tensile stress

Si thin film

Fixed

Mineralized collagen/PCL scaffold

10 mm

B

w/ Si

w/o Si

Stress (MPa)
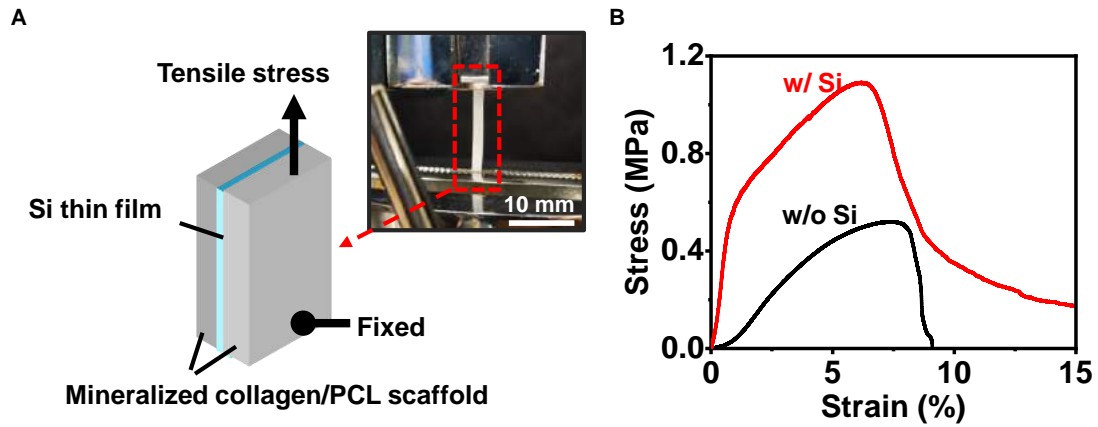
Strain (%)

Fig. S3. Mechanical characterization of scaffolds. (**A**) Schematic illustration and optical image for the mechanical testing setup. (**B**) Measured strain-stress curves for 3D scaffolds with and without embedded Si films.

Fig. S4.
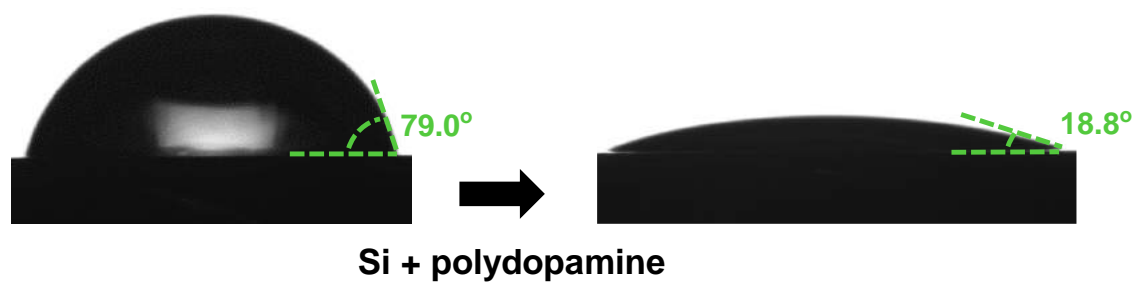
Si + polydopamine

Fig. S4. Wetting properties of Si surfaces. Photographs showing contact angles for water droplets on Si surfaces before (left) and after (right) polydopamine coating for 30 min.

Fig. S5.
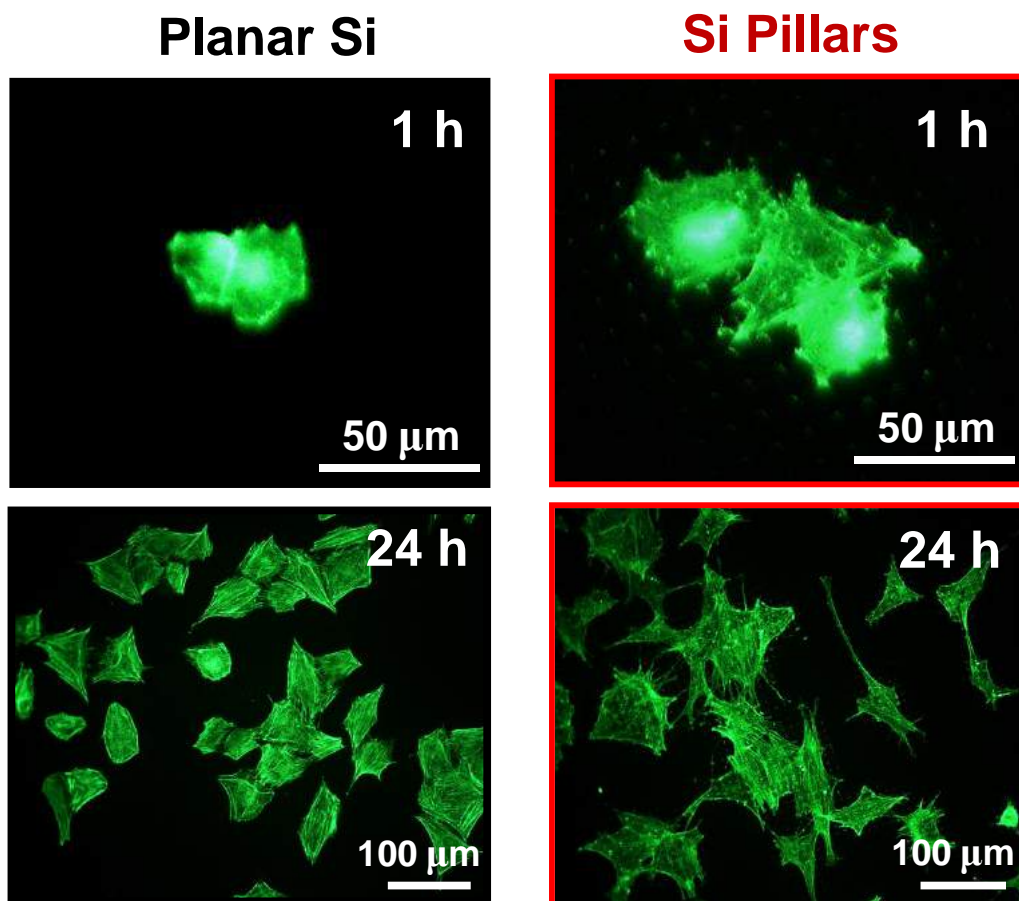
Fig. S5. Fluorescent images of MC3T3-E1 cells. These cells are cultured on planar Si (left) and Si pillars (right) after seeded for 1 h and 24 h, green: actin cytoskeleton.
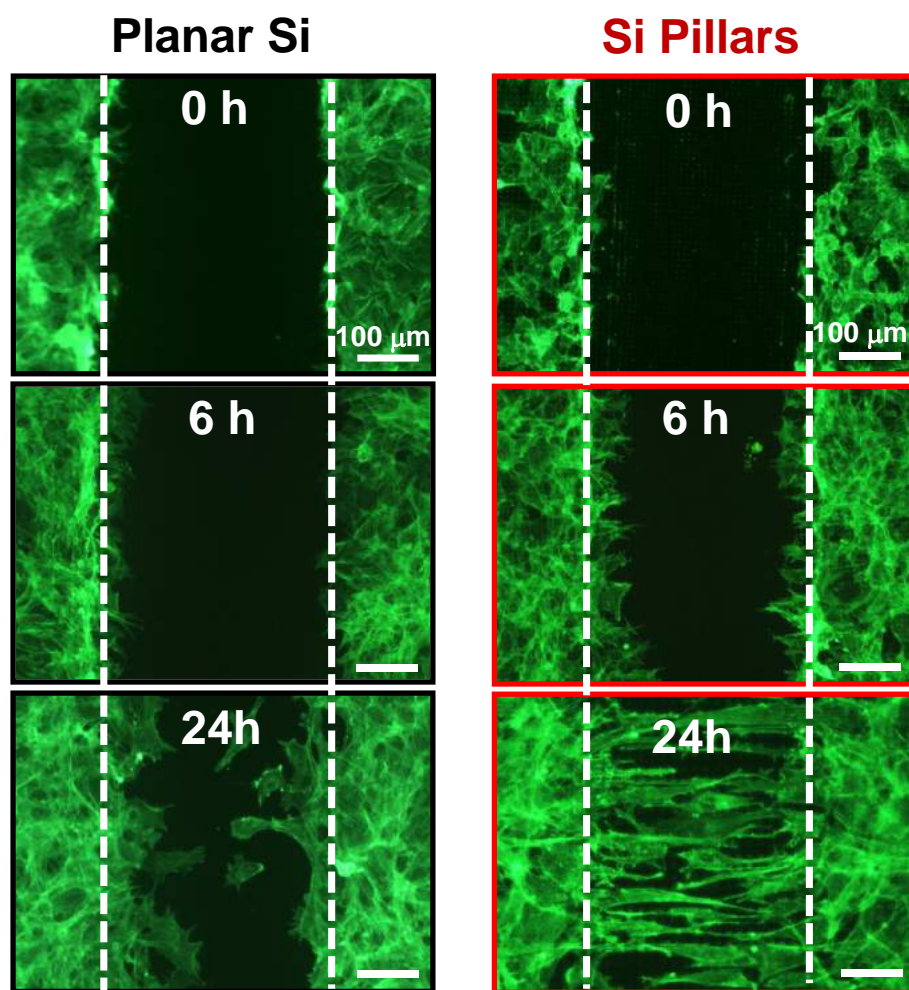
Fig. S6. Fluorescent images demonstrating migration behaviors of MC3T3-E1 cells. These cells are cultured on planar Si (left) and Si pillars (right) after seeded for 0 h, 6 h and 24 h, green: actin cytoskeleton.

Fig. S7.
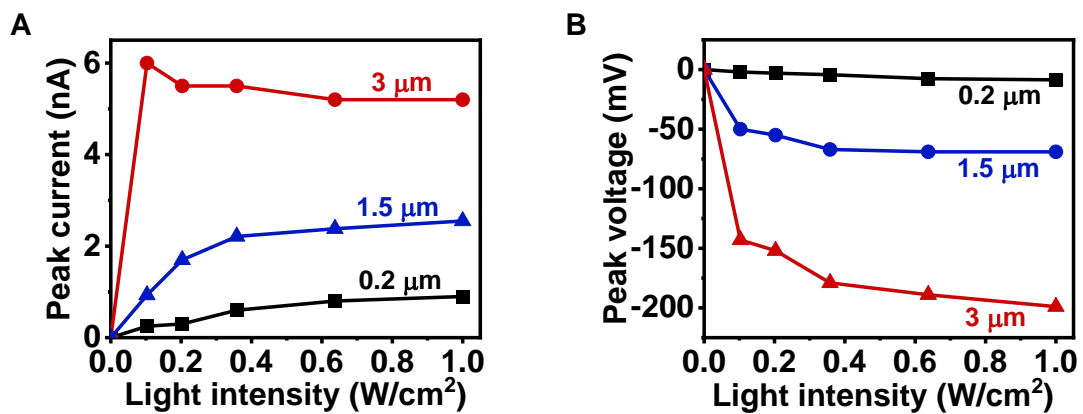
Fig. S7. Optoelectronic properties of Si films with various thicknesses. Measured peak current (**A**) and peak voltage (**B**) versus light intensity for Si films with thicknesses of 0.2 μm, 1.5 μm and 3 μm.

Fig. S8.
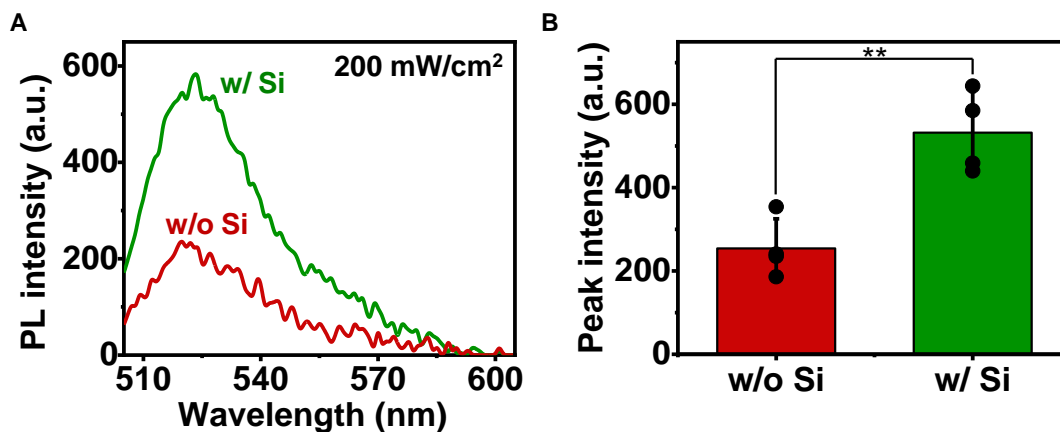
Fig. S8. Photoelectrochemical response of Si films. (**A**) Recorded photoluminescence (PL) spectra for 2,7-dichloro-dihydro-fluorescein, (DCFH) in PBS solution, under optical illumination (808 nm, power 200 mW/cm^2, duration 3 mins). The signals indicate the increased level of ROS on Si samples. (**B**) Statistical results showing peak PL intensity for solutions with and without Si samples. Results are presented as means $\pm$ s.e.m ($n = 4$ samples, ** $P < 0.01$).

Fig. S9.
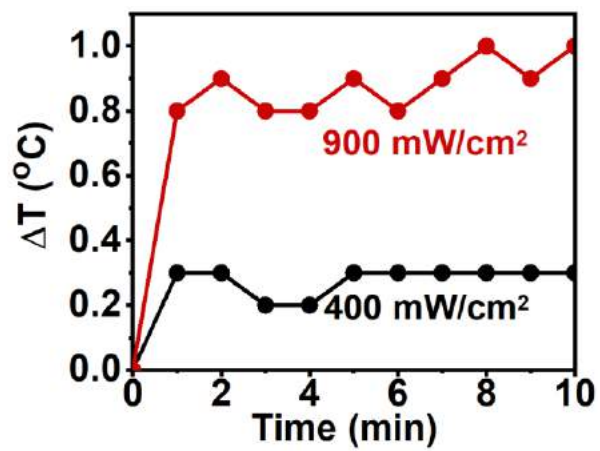
Fig. S9. Photothermal properties of Si films. Measured temperature rise of Si in PBS solution with a thermocouple exposed to 808 nm laser radiation (0.2 Hz, 3 s duration).

Fig. S10.
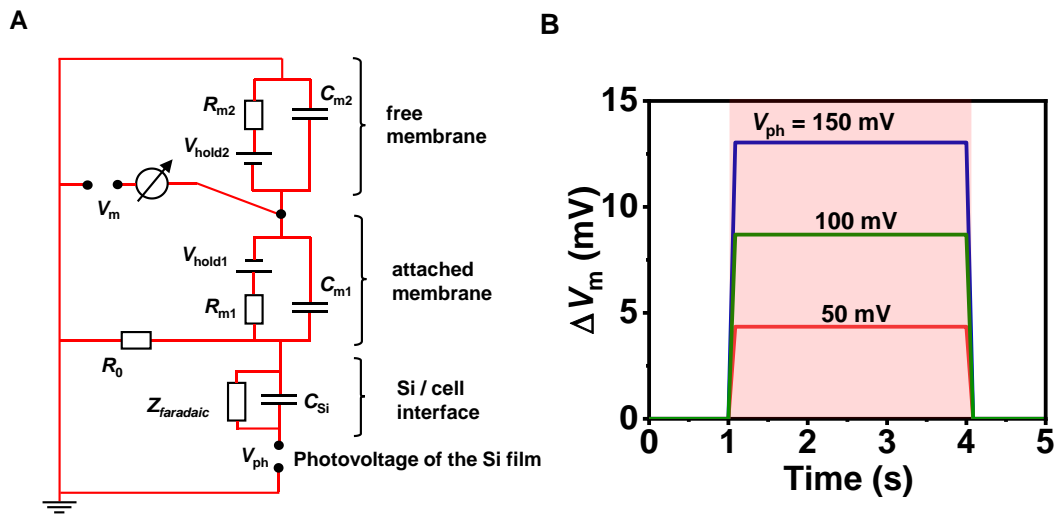
Fig. S10. Numerical simulation of the Si/cell interface. (A) Circuit model established to demonstrate the cellular depolarization by photostimulation. (B) Calculated membrane voltage changes (ΔV_m) responding to different photovoltages (V_{ph}) generated by Si. Here we assume the cell has a hemispheric shape with a spread area of 1500 μm^2. R_{m1} = 66.9 MΩ, R_{m2} = 33.45 MΩ, C_{m1} = 27.3 pF, C_{m2} = 54.6 pF, C_{Si} = 70.7 pF and $Z_{faradaic}$ = 8 MΩ. The initial holding potential V_{hold1} = V_{hold2} = −30 mV.

Fig. S11.
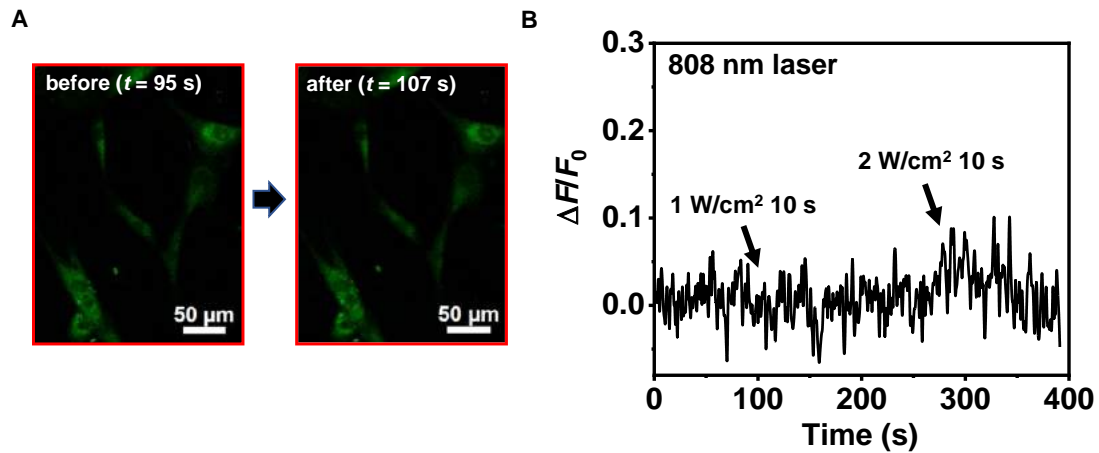
Fig. S11. Calcium activities for hBMSCs on glass. (**A**) Confocal microscopic images showing of hBMSCs on glass before and after laser stimulation. (**B**) Intracellular Ca^{2+} flux ($\Delta F/F_0$) measured under illumination with strong radiation intensities. No obvious Ca^{2+} spikes are observed.
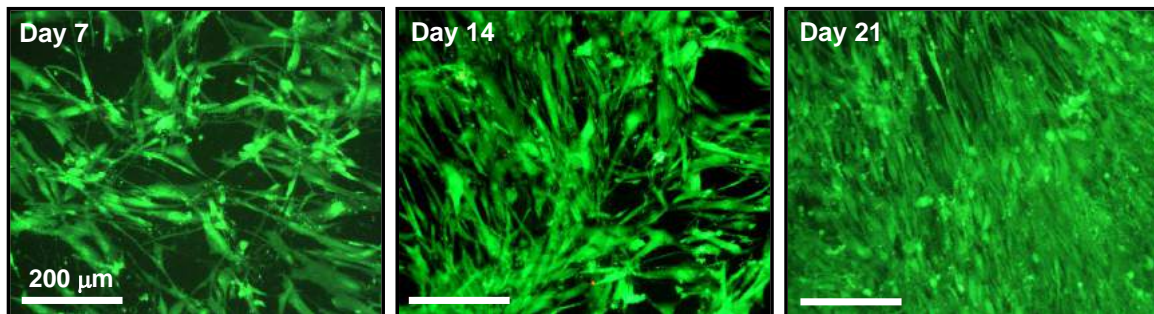
Fig. S12.

Fig. S12. Phototoxicity characterization. Fluorescent images showing the chronic biocompatibility of Si pillars under 808 nm laser illumination (200 mW/cm^2, 0.2 Hz, duration 3 s, 20 min every other day), examined by conducting cell live (green) / dead (red) staining tests.

Fig. S13.
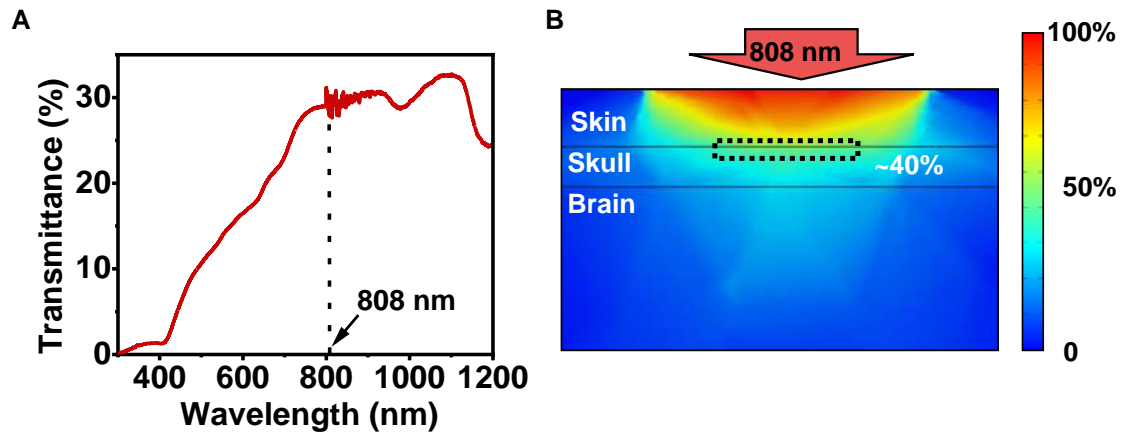
Fig. S13. Optical properties of biological tissues. (**A**) Measured transmission spectrum of the rat skin tissue (thickness ~2 mm). (**B**) Simulated light intensity distribution for 808 nm laser incident on the living tissue. The thickness of the skin is 2 mm.

Fig. S14.
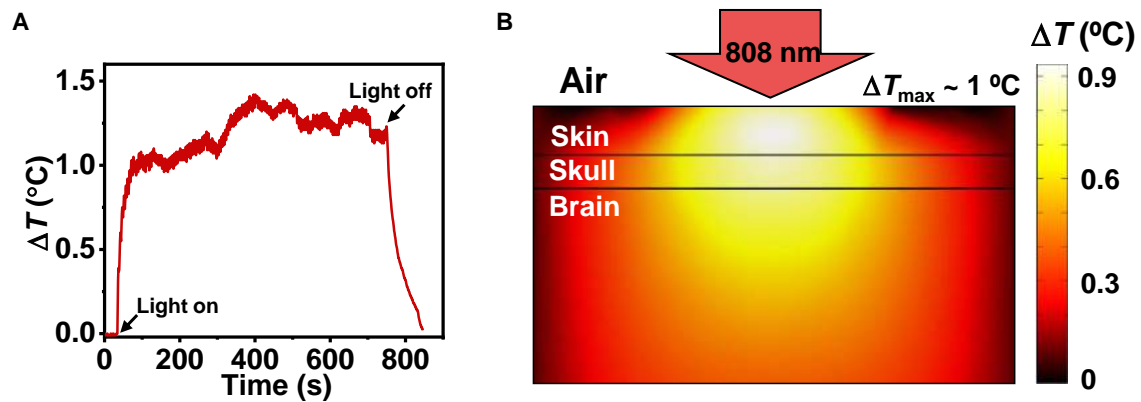
Fig. S14. Photothermal response of biological tissues. (**A**) Measured temperature rise under rat skin with a thermocouple exposed to 0.8 W/cm^2, 3s duration 0.2 Hz light radiation. (**B**) Simulated temperature distribution of tissue samples irradiated with an 808 nm laser at 0.8 W/cm^2.
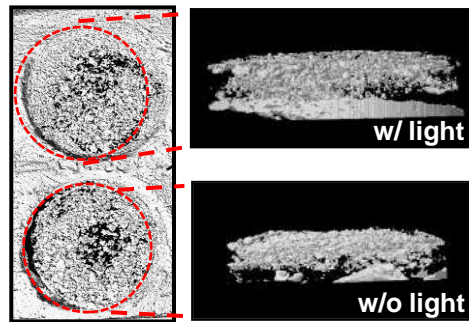
Fig. S15.

Fig. S15. Micro-CT images showing the radiological analysis of bone samples collected 4 weeks post implantation, (left: top view; right: side view).
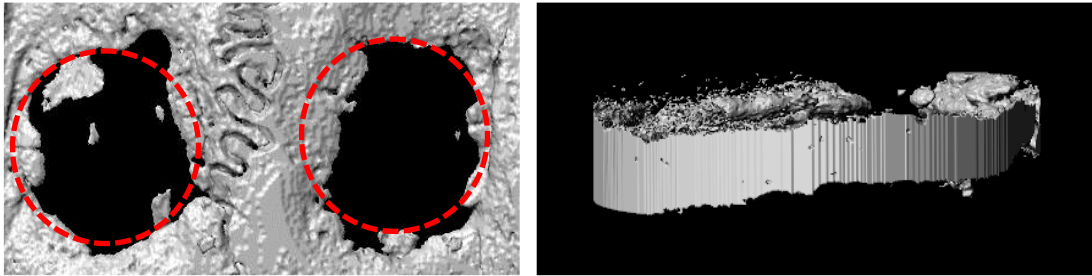
Fig. S16.

Blank: without scaffold

Fig. S16. Micro-CT images showing cranial defects in a rat without 3D scaffolds 8 weeks post surgery. Left: top view; Right: side view.
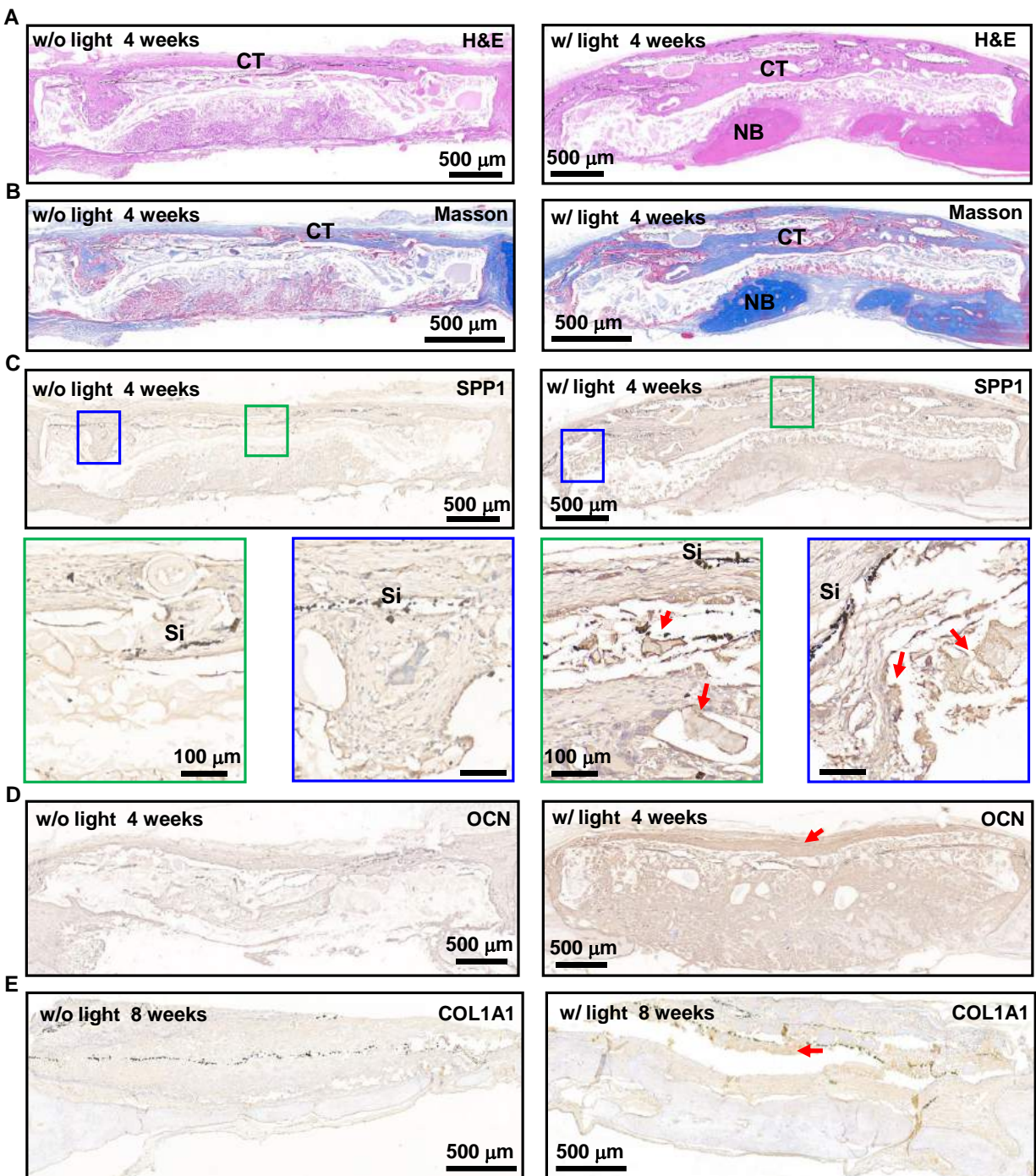
Fig. S17.

Fig. S17. Histological staining results. (**A**) H&E staining, (**B**) Masson staining and immunohistological staining of (**C**) SPP1, (**D**) OCN and (**E**) Col1A1 images of regenerated bone tissues with 3D scaffolds 4 weeks and 8 weeks post implantation. NB: newly formed bone, CT: connective tissues.
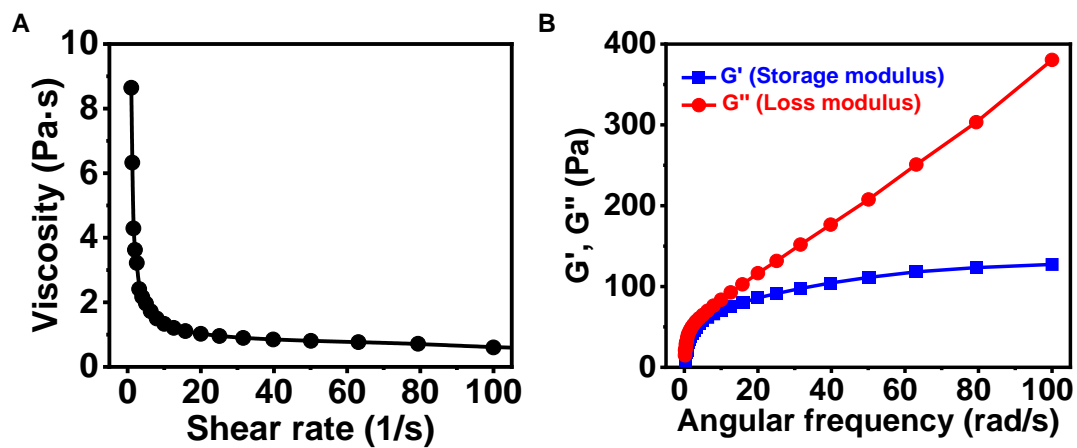
Fig. S18.

Fig. S18. Rheological properties of the slurry. (**A**) Measured viscosity versus shear rate for the slurry. (**B**) Storage modulus G′ (blue) and loss modulus G″ (red) versus angular frequency for the slurry. Results are measured at 25 ºC.